

University of Magdeburg

Faculty of Computer Science



Bachelor Thesis

# Multiple Linked Views for the Exploration of Optical Coherence Tomographic Image Data to Evaluate the Cerebral Artery Wall

Author:

Kristin Baumann

1<sup>st</sup> February 2016

Advisors:

Prof. Dr.-Ing. Bernhard Preim

Dr.-Ing. Sylvia Glaßer

Department of Simulation and Graphics

Visualization Group

**Baumann, Kristin:**

*Multiple Linked Views for the Exploration of Optical Coherence Tomographic Image Data to Evaluate the Cerebral Artery Wall*  
Bachelor Thesis, University of Magdeburg, 2016.

# Abstract

This bachelor thesis deals with the processing of image data for specific parts of the cerebral vasculature acquired by optical coherence tomography (OCT) in order to combine the data with visualisations of these structures in a multiple linked view framework.

More precisely, it describes the extraction of 3D triangle surface meshes from OCT data of the Circle of Willis to evaluate the cerebral artery wall. The 3D surface meshes are employed for an interactive 3D view, where parameters like the vessel radius and the vessel wall thickness are color-coded with a bivariate color mapping.

The Circle of Willis forms a major component of the cerebral circulation to supply the brain with blood. Cerebrovascular diseases like aneurysms or stroke can occur in this cerebral arterial circle, which are often characterised by a pathological change of the cerebral artery wall. Since conventional imaging modalities like MRI and CT cannot acquire the vessel wall with its layers, this rare information can be gained by using OCT.

The resulting visualisation is presented in a graphical user interface where it is linked to the original OCT slices. In summary, the software prototype allows a detailed exploration and evaluation of the cerebral artery wall, which provides indications for the detection of various cerebral diseases.



# Acknowledgements

I like to thank my advisors Dr.-Ing. Sylvia Glaßer and Prof. Dr.-Ing. Bernhard Preim for giving me the opportunity to write this thesis and implement the related software prototype. Without Sylvia's excellent support, this work would not have been possible in this scope.

This work was supported by the *Forschungscampus STIMULATE (Solution Centre for Image Guided Local Therapies)* in Magdeburg, Germany.



# Contents

<b>List of Figures</b>	<b>x</b>
<b>List of Acronyms</b>	<b>xi</b>
<b>1 Introduction</b>	<b>1</b>
<b>2 Fundamentals</b>	<b>3</b>
2.1 Cerebrovascular Diseases . . . . .	3
2.2 Anatomy of the Circle of Willis . . . . .	5
2.3 Risk Assessment Based on Internal Blood Flow and Vessel Wall Thickness	9
2.4 Concept of Multiple Linked Views for the Exploration of OCT Image Data to Evaluate the Cerebral Artery Wall . . . . .	12
<b>3 Realisation</b>	<b>15</b>
3.1 Implementation Overview . . . . .	15
3.2 Generation of a 3D Circle of Willis Model . . . . .	19
3.2.1 Adaption of the 2D Circle of Willis Scheme . . . . .	19
3.2.2 Measuring of 3D Positions from the MRI Dataset . . . . .	21
3.3 Adaptation of the 3D Circle of Willis Model to OCT Data . . . . .	22
3.3.1 Measuring OCT Datasets . . . . .	22
3.3.2 Fitting of Segment Lengths to the Model . . . . .	23
3.4 Calculation of 3D Surface Meshes . . . . .	27
3.4.1 Point Generation . . . . .	27
3.4.2 Treatment of Segment Junctions and Mesh Processing . . . . .	29
3.4.3 Calculation of Vessel Diameter and Wall Thickness . . . . .	32
3.5 Multiple Linked View Framework . . . . .	34
3.5.1 Loading of the Surface Meshes and the OCT Image Data . . . . .	36
3.5.2 Color-coded 3D Visualisation of the Triangle Surface Meshes . . . . .	36
3.5.3 Linking the 3D Surface Mesh View with the 2D OCT Slice View	39
<b>4 Discussion</b>	<b>41</b>
<b>5 Summary</b>	<b>45</b>
<b>A Appendix</b>	<b>47</b>
<b>Bibliography</b>	<b>51</b>



# List of Figures

2.1	Arteries of the brain . . . . .	5
2.2	Schematic representation of the Circle of Willis . . . . .	7
2.3	Schematic representation of the variants of the Circle of Willis . . . . .	8
2.4	Structure of the artery wall . . . . .	10
2.5	OCT setups for the inspected Circle of Willis . . . . .	13
2.6	Circle of Willis specimen explanted post mortem during OCT image acquisition . . . . .	13
2.7	Lateral View of the Circle of Willis reconstructed from the MRI data .	14
3.1	Data processing pipeline . . . . .	17
3.2	Components of the visualisation forming the VesselWallExplorer . . . .	18
3.3	Specific adaption of the Circle of Willis scheme at the junctions of the internal carotid artery . . . . .	19
3.4	Advanced schematic representation of the Circle of Willis . . . . .	20
3.5	General model of the Circle of Willis . . . . .	21
3.6	Measurement of the OCT slices . . . . .	22
3.7	Approximation of the vessel shape . . . . .	23
3.8	Outline of the calculation of the intersecting plane of two spheres . .	24
3.9	Outline of the center calculation of the intersecting circle . . . . .	25
3.10	Outline of the radius calculation of the intersecting circle . . . . .	25
3.11	Adapted model of the Circle of Willis . . . . .	26
3.12	Outline of the linear interpolation and sampling of the 3D circle for the mesh generation . . . . .	28
3.13	First mesh building approach at the segment junctions . . . . .	29

3.14	Second mesh building approach at the segment junctions . . . . .	30
3.15	Post-processed mesh of the inner vessel wall border . . . . .	31
3.16	First approach of calculating the vessel radius . . . . .	32
3.17	Second approach of calculating the vessel radius . . . . .	33
3.18	Multiple linked view framework <i>VesselWallExplorer</i> . . . . .	35
3.19	GUI component: loading of the meshes and the OCT image data . . .	36
3.20	GUI component: first approach of the parameter color-coding . . . .	37
3.21	GUI component: second approach of the parameter color-coding . . . .	38
3.22	GUI component: 2D OCT slice views with interaction elements . . . .	39
3.23	GUI component: glyph highlighting the current slice position . . . . .	40
4.1	Bivariate histogram showing the parameter distribution of the vessel radius and the vessel wall thickness . . . . .	42
A.1	View from below of the Circle of Willis reconstructed from the MRI data	47
A.2	Data table of OCT measurement results . . . . .	48
A.3	Post-processed mesh of the outer vessel wall border . . . . .	49

# List of Acronyms

<b>A1</b>	Segment A1 of the anterior cerebral artery
<b>ACA</b>	Anterior cerebral artery
<b>AComm</b>	Anterior communicating artery
<b>BA</b>	Basilar artery
<b>C6</b>	Segment C6 of the internal carotid artery
<b>C7</b>	Segment C7 of the internal carotid artery
<b>GUI</b>	Graphical user interface
<b>ICA</b>	Internal carotid artery
<b>IVUS</b>	Intravascular ultrasound
<b>M1</b>	Segment M1 of the middle cerebral artery
<b>MCA</b>	Middle cerebral artery
<b>OCT</b>	Optical coherence tomography
<b>P1</b>	Segment P1 of the posterior cerebral artery
<b>PCA</b>	Posterior cerebral artery
<b>PComm</b>	Posterior communicating artery
<b>VA</b>	Vertebral artery



# 1. Introduction

The Circle of Willis forms, as a vital subnetwork of the cerebral vasculature, a main component of the cerebral circulation to supply the brain with blood. Diseases which can occur in this cerebral arterial circle, like stroke or aneurysms, are often sudden, and – as a worse case – fatal. Furthermore, the incidence of these diseases is high, since stroke, for example, ranks with 6.7 million deaths in 2012 as the second most common cause of death worldwide [WHO14].

This motivates a extensive research activity in this topic, in particular by using diverse imaging modalities including, next to MRI, intravascular ultrasound (IVUS) and optical coherence tomography (OCT). The latter with its superior spatial resolution is already successfully used in cardiology, while for cerebral arteries the admission of the medical board is still expected. Intravascular imaging shows, in contrary to the other modalities, the vessel wall with its layers and borders, which provides significant indications for the detection of various cerebral diseases.

For potential clinical use, a sophisticated visualisation of the initial image data can reduce the evaluation effort and guide medical experts to potential pathologies. An interactive visualisation facilitates the exploration and therefore the possibility to gain insights through additional presentation of essential parameters.

This issue is addressed by the present thesis as it introduces a graphical user interface for the exploration of OCT data of the Circle of Willis based on the visualisation of 3D triangle surface meshes of the inner and outer vessel wall border, which simultaneously represents the vessel radius and vessel wall thickness.

In summary, the contributions of this thesis are the following:

- Extraction and reconstruction of 3D triangle surface meshes of the inner and outer vessel wall border from OCT image data of cerebral arteries.
- Simultaneous, color-coded display of the vessel radius and the wall thickness in the 3D visualisation of the vessel walls.
- A multiple linked view framework including the underlying OCT slices for the visual exploration.

This thesis is structured as follows: **Chapter 2** explains the fundamental bases determining the subsequent realisation of the software. It covers the medical background, which includes characteristics of diseases occurring in the cerebral vessels as well as the general anatomy of the Circle of Willis. This is followed by a brief comment about the risk assessment of these diseases in the cerebral arterial circle by means of different imaging modalities, which leads to a detailed presentation of the objective of this thesis.

**Chapter 3** explains the realisation of the multiple linked view framework. After an overview of the implementation process, the individual steps from the OCT image data to the vessel wall meshes and to the rendered visualisations in the user interface are clarified and enhanced by mathematical descriptions and illustrations of the intermediate findings.

A critical evaluation of the results is drawn in **Chapter 4** including remarks on future work, before the thesis closes with a conclusion in **Chapter 5**.

## 2. Fundamentals

### 2.1 Cerebrovascular Diseases

Cerebrovascular diseases comprise a group of diseases affecting the blood vessels of the brain, particularly the cerebral arteries and cerebral veins. This includes some of the most common and significant disease patterns as described below.

Cerebrovascular diseases can be divided into three main categories: cerebral infarctions, intracranial hemorrhages, and vascular malformations like cerebral aneurysms and arteriovenous malformations [GEE12]. This general categorization is not absolute, as the particular disorders are mutually dependent.

Cerebral infarction, also known as ischemic stroke or white stroke, describes a sudden insufficient blood supply of the brain and thereby causing an undersupply of oxygen and glucose. The reduced blood circulation is mostly caused by stenosis, an abnormal narrowing or closure in a brain-supplying artery. In the majority of cases the stenosis results from arteriosclerosis which comprises thickening, hardening and loss of elasticity of the vessel walls due to the sedimentation of fats, cholesterol and other substances in and on the walls. These plaques lead to a reduction of the vessel lumen. The shortage of oxygen, called ischemia, causes irreversible tissue damage within minutes and progresses quickly to necrotic tissue [HSD10].

The second category, intracranial hemorrhages, refer to the leakage of blood. If the bleeding occurs within the brain, it is called intracerebral hemorrhage, otherwise it is called subarachnoid hemorrhage if the leak is between the inner and outer layers or the tissue covering the brain. The bursting of a weakened vessel and the following blood loss induces a sudden increase in pressure within the brain, because the skull – being a bony structure – cannot expand [AHDT14]. The enhanced pressure damages the sensitive nerve tissue. If the hemorrhage exceeds a certain limit, irreversible damage of the brain substance and neurological failures are expected to occur in a short amount

of time. The most frequent risk factor for intracranial hemorrhages, and subsequent hemorrhagic strokes, is high arterial pressure, which may cause, along with a weakened wall, the rupture of the vessel [ISCb].

The third and last category, called vascular malformations, includes cerebral aneurysms. An aneurysm occurs at a weak section of a vessel wall that balloons out and fills with blood. About 86% of the intracranial aneurysms arise in the anterior part of the brain blood circulation and are often found at the bifurcations of the main arteries [BTP<sup>+</sup>]. The modification of the inner vessel wall can be invoked by both acquired and inborn factors, that lead, alongside with the narrowing of arteries and high blood pressure, to the expansion. With an increasing extent the bulging aneurysm may leak or rupture, leading to a hemorrhage in the surrounding tissue and in consequence to a hemorrhage stroke [oNDS13].

The described disorders form a extremely dangerous group of diseases as they are characterised by a sudden occurrence and a mostly fatal outcome. There are several studies which show the fatal impact of these diseases. The World Health Organisation (WHO) states stroke as the second most common cause of death with 6.7 million deaths worldwide in 2012 [WHO14]. Furthermore stroke is the most frequent reason for acquired disability and care dependency in old age [HBW<sup>+10</sup>]. Stroke accounts for 8% of all deaths, making it - after infarction and cancer diseases - the third most common cause of death in Germany. In 2008, 63.000 deaths were registered in the official causes of death statistics [Bun10]. Ischemic strokes formed the largest proportion, comprising 80% of all strokes [HBW<sup>+10</sup>].

## 2.2 Anatomy of the Circle of Willis

The diseases described in Section 2.1 occur mostly in the main brain arteries which compose the cerebral arterial circle, also known as Circle of Willis. The following section describes its components and characteristics in context of the cerebral circulation.

The arterial blood supply to the brain consists of two pairs of large arteries: the left and right *internal carotid artery* (ICA) as well as the left and right *vertebral artery* (VA). The *vertebral arteries* converge and form the *basilar artery* (BA). This main artery joins subsequently the two *internal carotid arteries* and other communicating arteries to form a ring-shaped structure at the base of the brain, named Circle of Willis. The arterial cerebral circulation can be divided into anterior and posterior cerebral circulation which are connected via bilateral *posterior communicating arteries* (PComm). Three pairs of arteries arise basically from the Circle of Willis - the *anterior cerebral artery* (ACA), the *middle cerebral artery* (MCA) and the *posterior cerebral artery* (PCA). These arteries split progressively up into smaller arteries that proceed until they enter the brain tissue and supply the according regions of the cerebral cortex with blood [Cip09]. The described anatomy is shown in Figure 2.1.

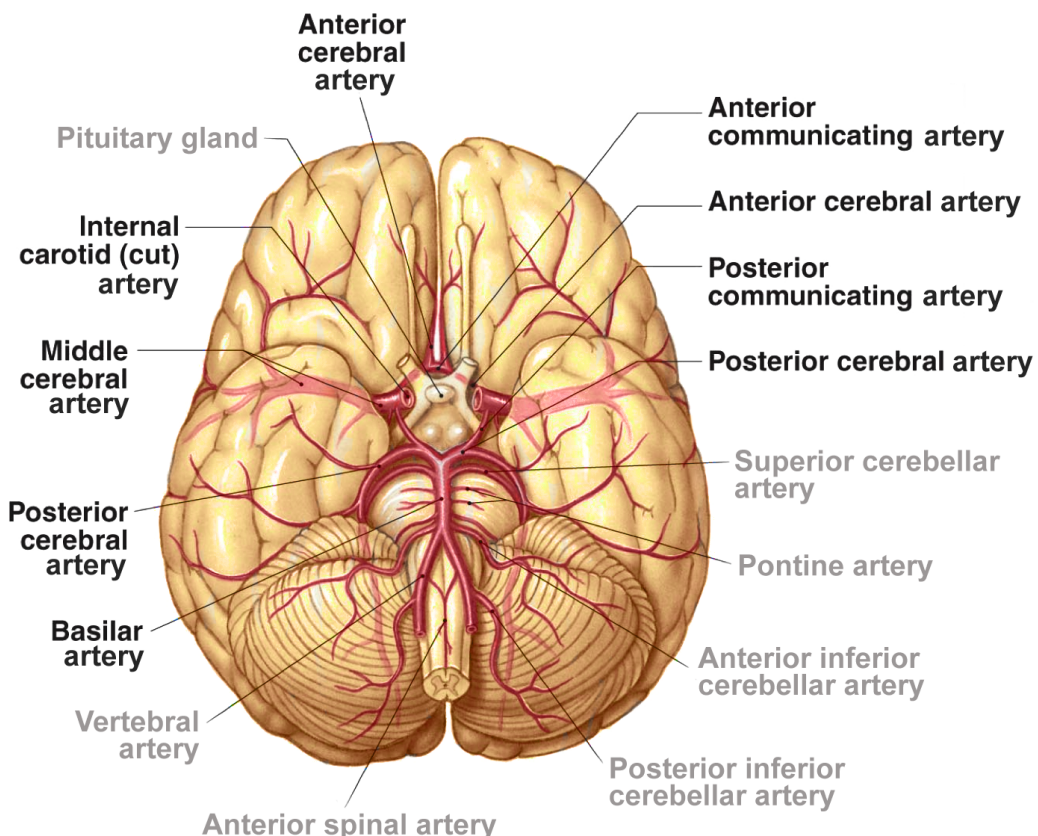


Figure 2.1: Illustration of the arteries of the brain (viewed from below) where the components of the Circle of Willis are labelled in black (adapted from [Mar09]).

For the subsequent investigation of the Circle of Willis, a finer subdivision of the single arteries is necessary, because only certain segments of the previously mentioned vessels form the cerebral arterial circle. Several classification schemes have been described for those. Due to its appropriate level of detail, this work is based on the numbering and acronym system employed by Harrigan and Deveikis in [HD09]. Figure 2.2 on page 7 shows a schematic representation of the Circle of Willis with labelled segments:

- **Basilar artery.** The BA arises, as stated previously, from the confluence of the two VAs, then continues mostly straight until it divides into the paired PCAs.
- **Posterior cerebral arteries.** The PCAs emerge from the BA at the basilar artery bifurcation. Segment P1 runs from this bifurcation to the junction with the PComm. Segment P2 continues to the posterior aspect of the midbrain. The PCAs eventually supply oxygenated blood to the posterior aspect of the brain, more precisely the occipital lobe.
- **Posterior communicating arteries.** The PComms establish the connection between the anterior and posterior cerebral circulation, because they link the PCA with the ICA, before terminating in the bifurcation of the ICA into the ACA and MCA.
- **Internal cerebral arteries.** The ICAs result from the common carotid arteries running on each side of the head and neck. Further along the vessel, Segment C6, also called ophthalmic segment, ends at the origin of the PCA. Segment C7, the communicating segment, begins at the origin of the PCA and ends with the bifurcation of the ICA into the ACA and the MCA.
- **Middle cerebral arteries.** The MCAs arise from the trisection of ICA and represent a major blood supply of the cerebrum. Therefore, segment M1, starting at the ICA, is considered part of the Circle of Willis in this work, even though in some literature, the MCA is only seen as a direct continuation of the ICA.
- **Anterior cerebral arteries.** The ACAs emerge from the ICAs. The two ICAs are connected via the anterior communicating artery (AComm). Hence, Segment A1 proceeds from the ICA to the separation to the AComm. From this crossing, Segment A2 continues. In general, the ACAs supply most of the anterior part of the brain.
- **Anterior communicating artery.** The AComm links the left and right ACA and closes thereby the cerebral artery circle.

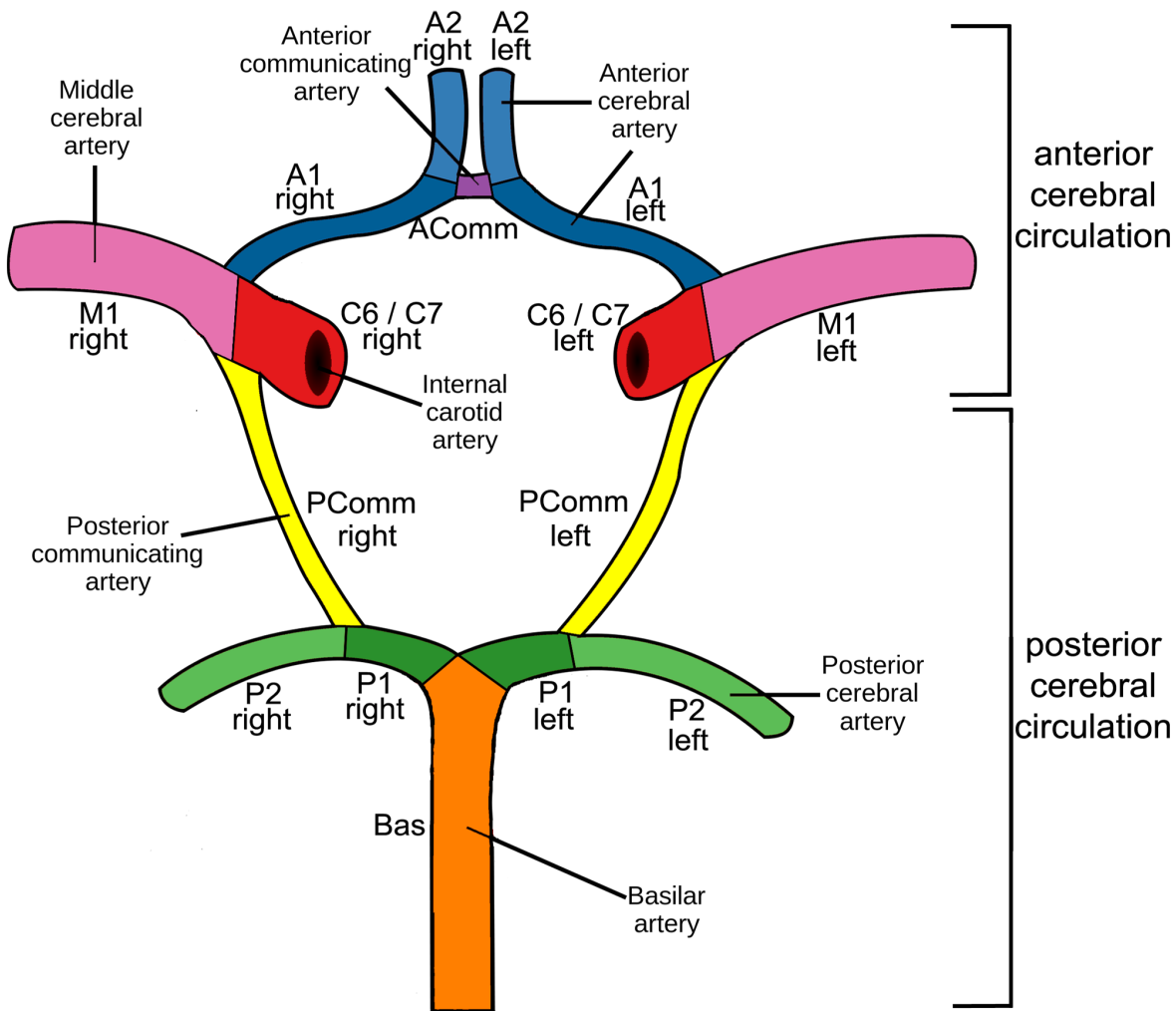


Figure 2.2: Schematic representation of the Circle of Willis (based on [Com]).

The arrangement of the arteries in a circle, or more precisely as a nine-sided structure, creates redundancies in the cerebral circulation. If one artery possesses a stenosis or is even occluded, blood flow from the other vessels can maintain the cerebral perfusion. This so-called collateral circulation supplies the distal smaller arteries, which would be otherwise cut off [ISCa].

However, it has become evident that in about half of the cases the Circle of Willis is not well-developed and symmetric, but shows a certain variant congenitally [HMA13]. The variations can appear as underdeveloped, narrowed vessels, denoted as hypoplasia, or as completely absent, denoted as aplasia. Hashemi et.al. characterise in [HMA13] common variants which can be seen in Figure 2.3. Thereby, vessels with a diameter less than 1 mm were marked as hypoplasia. Sketch A shows the normal vascular pattern as a reference, sketch B the hypoplasia of the ACA, sketch C the unilateral hypoplasia of the ACA A1 segment, sketch D the unilateral aplasia of PCA, sketch E the bilateral aplasia of the PComm, sketch F the unilateral hypoplasia of the PComm and sketch G the bilateral hypoplasia of the PComm. This enumeration illustrates already that the PComm, as the connection of the two parts of the cerebral circulation, is most frequently subject to variations, next to the AComm and A1 segment, as shown in several studies [HD09, HMA13].

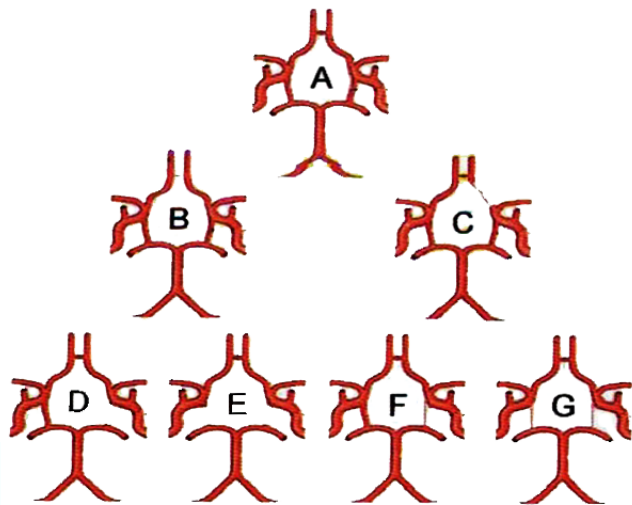


Figure 2.3: Schematic representation of the most frequent variants of the Circle of Willis (from [HMA13]).

If a component of the cerebral artery circle is hypoplastic, the capacity of collateral supply is diminished. Implicitly, the asymmetry of the Circle of Willis has a direct impact upon the distribution of carotid and basilar blood flow. Hence, patients with aneurysms are more likely to possess an abnormal circle [HD09]. In summary, the Circle of Willis and its variations play an important role in the development of cerebrovascular diseases.

## 2.3 Risk Assessment Based on Internal Blood Flow and Vessel Wall Thickness

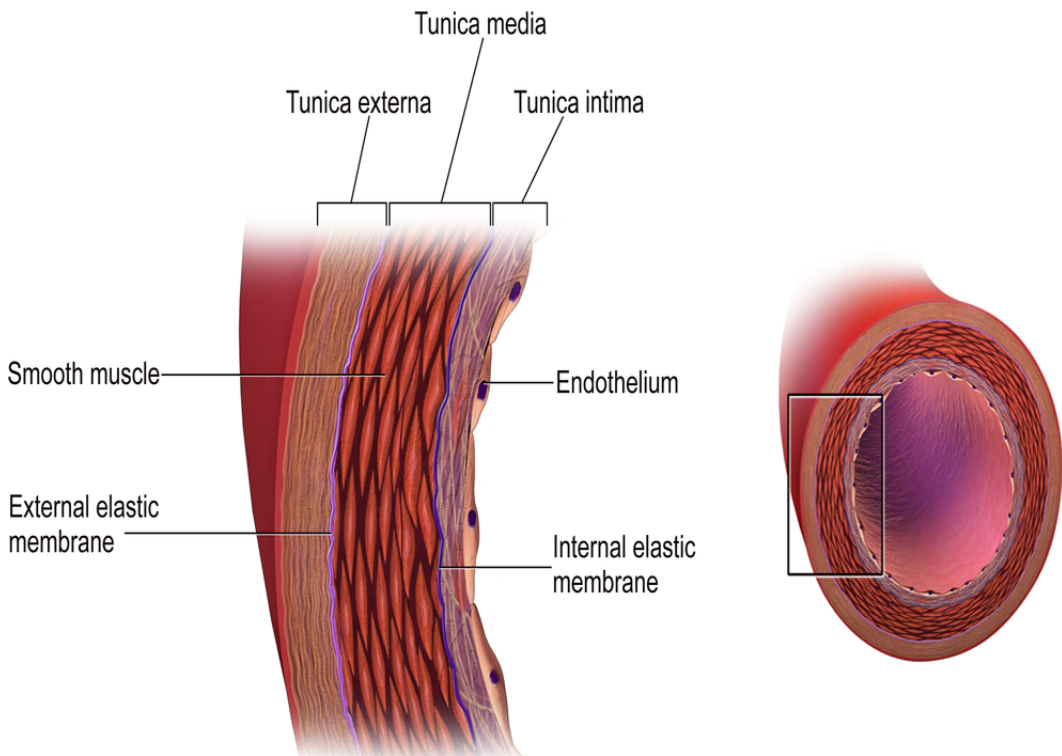
The cerebrovascular diseases at the Circle of Willis are characterised by a high incidence, a mostly fatal outcome and a sudden occurrence, as described in Section 2.1. Therefore, a clear detection and sufficient assessment of the disorders and their causes are important for the indication of therapy.

Certain linked factors enhance the risk in general. These include high blood pressure, atrial fibrillation, raised blood cholesterol levels, diabetes and an unhealthy way of life with enhanced smoking, alcohol abuse or obesity [NIH15]. In consequence, these causes affect the internal blood flow behaviour in the vessel as well as the condition of the vessel wall.

The former establishes the basis for the risk analysis of cerebrovascular diseases, e.g., aneurysms, as the flow depends on elemental fluid dynamic parameters like geometry and elasticity of the vessel, blood pressure and volume as well as flow velocity. On the one hand, the blood flow can be directly measured by the means of 4D phase contrast magnetic resonance imaging. On the other hand, the blood flow information can be approximated via computational fluid dynamic (CFD) simulations on a 4D volumetric grid. However, for an enhanced patient-specific disease assessment and, in consequence, for a precise therapy indication the sole inspection of internal blood flow in the suspect vessel is not sufficient, because it is, amongst others, strongly influenced by the wall condition like the wall thickness.

For example, when considering the risk of a hemorrhage, a fully developed vessel wall with an adequate thickness can compensate an increased wall shear stress, whereas a fragile thin wall bearing the same strain is more likely to burst. The importance of an accurate risk assessment and therefore a detailed observation of the wall morphology is also reflected when facing the treatment decision of incidentally detected intracranial aneurysms. Due to the psychological burden arising from the anxiety associated with the risk of rupture, the patient may prefer interventional treatment associated with equal or higher risk of complication compared to a conventional wait-and-see strategy.

Since cerebrovascular diseases often affect the vessel wall, e.g., in case of arteriosclerosis or hemorrhages, as described in Section 2.1, the condition of the cerebral vessel wall has to be further observed. As shown in Figure 2.4 on page 10, the artery wall consists of three layers: the outermost layer *tunica externa*, the middle layer *tunica media* and the innermost layer *tunica intima*. This work concentrates on the inner wall border, separating the intima from the lumen, and the outer wall border, dividing the *externa* and the surrounding tissue, as well as on the vessel wall thickness as the distance between these two components.



"Structure of an Artery Wall" by Bruce Blaus, used under CC BY 3.0

Figure 2.4: Structure of the artery wall showing its three layers *tunica intima*, *tunica media* and *tunica externa* (adapted from [Bla]).

Medical imaging of the vessel wall can be performed in different ways. Current research has shown that the wall can be represented by high-resolution magnetic resonance imaging [CJL15, LO14]. This is performed with MR clinical research instruments using 7 T, in contrast to 1.5 to 3 T diagnostic devices in clinical practice. Moreover, these high-resolution devices allow a detailed display of the vessel wall borders, however, the resolution is not sufficient to distinguish between the three artery wall layers.

This can be achieved by intravascular imaging methods like intravascular ultrasound (IVUS) and, more recently, optical coherence tomography (OCT), as they are already utilized in the clinical routine for cardiology [RTT<sup>+</sup>11]. Especially OCT introduces the opportunity to assess characteristics like vessel wall thickness or other morphological and structural features. While the analysis of the arterial walls based on intravascular imaging is primarily performed in cardiology, a similarly effective modality for cerebral vessels is still absent, since the *in vivo* use of OCT is not yet authorized for the cerebral vasculature.

However, current research proves the feasible use of OCT in context with cardiological and cerebral structures. Hoffmann et.al. showed the potential of OCT for the evaluation of intracranial aneurysms [HGB<sup>+</sup>15]. In [YKY<sup>+</sup>12], OCT was successfully employed to characterize atherosclerotic plaque in the larger carotid arteries. Mathews et.al. verified the clinical use of OCT for detecting arterial structures in the cerebral vasculature using animal and human vessels explanted postmortem [MSH<sup>+</sup>11]. In [GHB<sup>+</sup>15], OCT data was combined with histology data to further analyze the cerebral artery wall.

The restrictions of the medical board preventing the usage of OCT are expected to be dropped, as soon as the catheters are small and flexible enough for a safe *in vivo* use in the partly tiny cerebral vessels. The risk assessment of cerebrovascular diseases will strongly advance with this chance to characterise pathological vessel wall changes with a spatial resolution superior to other intravascular imaging methods [TMF<sup>+</sup>12].

## 2.4 Concept of Multiple Linked Views for the Exploration of OCT Image Data to Evaluate the Cerebral Artery Wall

As described in the previous section, the investigation of cerebral vessels with OCT as imaging modality is a current research area with great potential for improvement of the diagnosis and risk analysis of cerebrovascular diseases. This is taken up by the present thesis, as it describes the necessary steps to convert the OCT image data into an expressive 3D visualisation of the vessels of the Circle of Willis showing parameters needed for usage in a clinical setting. Within the scope of a multiple linked view framework, it allows the exploration of the OCT data for a detailed evaluation of the cerebral artery wall.

Several approaches for the visualization of vessels including their vessel wall have been examined in recent work. Direct volume rendering was used in [GOH<sup>+</sup>10], whereby the whole wall with pathologies like atherosclerotic plaque was automatically highlighted with adapted transfer functions. But the inner and outer vessel wall were not explicitly extracted. Balzani et al. used a reconstructed 3D model of atherosclerotic arteries to visualise parameter values color-coded on the inner wall together with a transparent outer wall. Furthermore, the framework included cross sections showing virtual histology data [BBB<sup>+</sup>12]. Glaßer et.al. combined the visualisation of the inner and outer wall of an artificially generated porcine aneurysm, showing the vessel wall thickness via distance ribbons, with hemodynamic information from a computational fluid dynamic (CFD) simulation. The shading was adapted such that the inner wall and its distance to the outer wall is always perceivable [GLH<sup>+</sup>14]. In [LGV<sup>+</sup>16], an approach with cutaway surfaces was introduced to illustrate blood flow pathlines and wall thickness information for an improved aneurysm treatment risk assessment.

Since OCT is not approved for cerebral arteries *in vivo* yet, this work is based on a human Circle of Willis that was explanted post mortem in accordance with the local ethics committee. The process of image acquisition and the actually used equipment is extensively explained by Hoffmann et. al. in [HGB<sup>+</sup>15]. In summary, three specimen were captured, each consisting of about 6 setups with an average length of 130 mm on 1024 slices with a pixel size of 15  $\mu\text{m}$  x 15  $\mu\text{m}$ . The slices show 2D cross-sectional images of the vessel wall and they are arranged in a volume dataset along the catheter axis. On page 13, Figure 2.5 outlines the different setups for a Circle of Willis, while Figure 2.6 displays a specimen during the image acquisition.

While acquiring images of an explant, the lack of an intact blood cycle leads to a deflation or even a collapse of the vessels, which cannot be completely prevented by flushing the vessel system with an injector system. The vessel shape is additionally altered by the catheter's stiffness when pulled back through the vessel parts, visible in Figure 2.6 on page 13. Furthermore, only segments with a diameter large enough to fit the catheter could be included in the measurements.

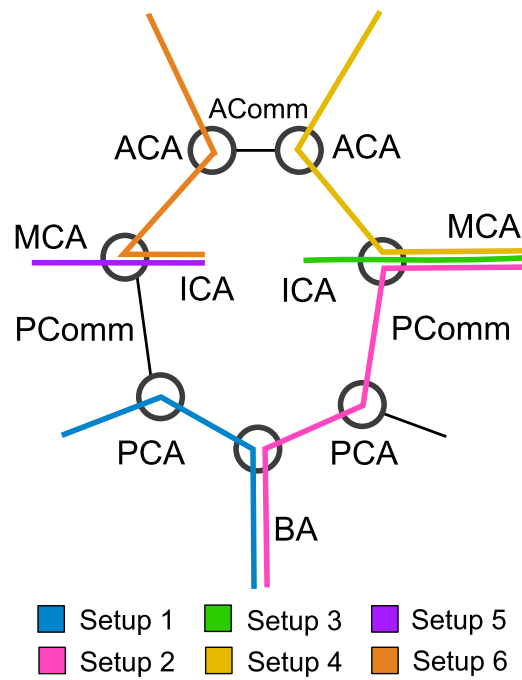


Figure 2.5: The six OCT setups for the inspected Circle of Willis (see Figure 2.2 for the vessel structure).

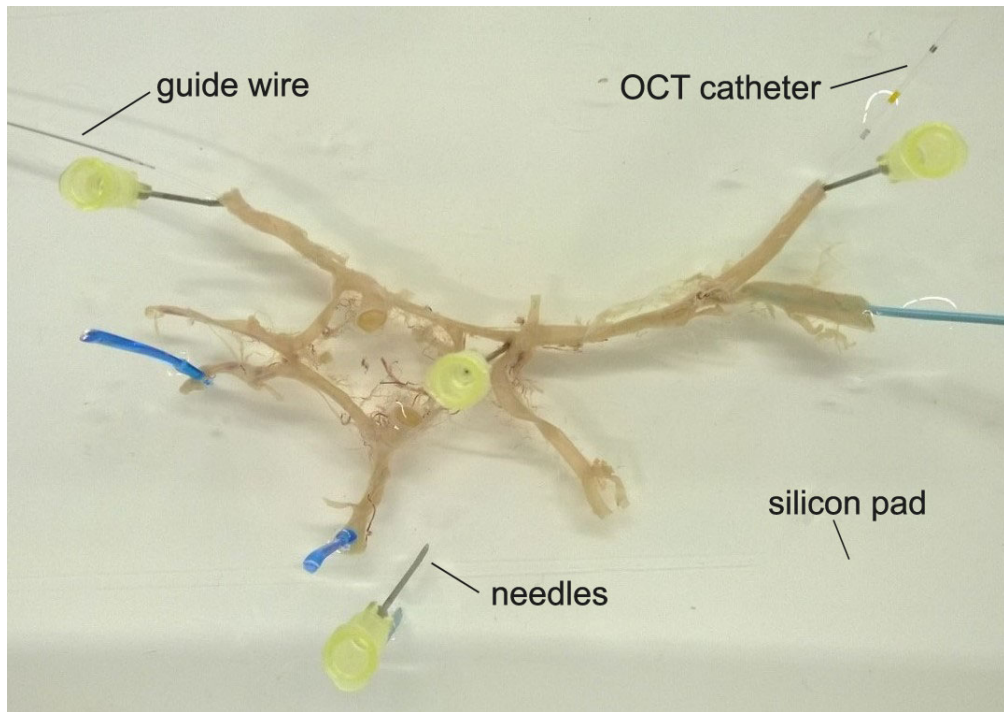


Figure 2.6: Circle of Willis specimen explanted post mortem during OCT image acquisition (measuring the BA, P1 left, PComm left and M1 left).

Due to the fact that the OCT data simultaneously depicts the inner and outer vessel wall as desired, but does not provide 3D spatial information necessary to generate a 3D visualisation, the OCT data was projected onto a 3D model extracted from a healthy patient's MRI dataset. The MRI data, visualised in Figure 2.7, has been acquired using the MAGNETOM Skyra 3T (Siemens Healthcare GmbH, Erlangen, Germany) combined with a 20ch-head/neck coil for internal use, e.g., clinical education or research projects. It does not provide the wall information, but the spatial extend can be extracted. Another view of the MRI data is provided in Figure A.1 in the appendix.

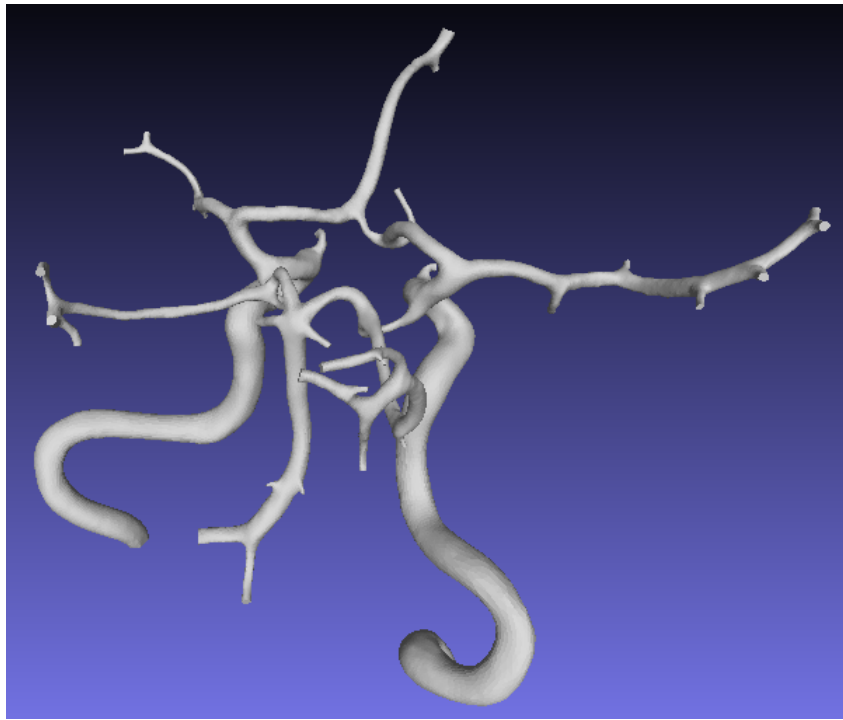


Figure 2.7: Lateral View of the Circle of Willis reconstructed from the MRI data displayed in MeshLab.

# 3. Realisation

## 3.1 Implementation Overview

The aim of this thesis, as clarified in the previous section, is the creation of a multiple linked view framework presenting the vessel system of the Circle of Willis with a focus on the vessel wall. It combines a 3D view of color-coded vessels with a display of the initial 2D cross-sectional OCT images. With regard to the objective, two related parameters are mapped: the vessel radius and the wall thickness as defined earlier. Therefore, the interactive tool allows an intensive exploration of the condition of the Circle of Willis by linking both depicted views. A general description of the realisation process follows, while the individual steps are explained in detail and with supporting illustrations in the next sections.

The underlying data basis is formed by the OCT setups with the depiction of the inner and outer wall and the MRI dataset with the 3D spatial information of the Circle of Willis. It is important to clarify that the vessel segments, in reality strongly curved, are approximated by straight cylinders for the moment, due to the missing curvature information in OCT slice data.

The implementation process can be divided in two main stages: the data processing turning the OCT and MRI datasets into 3D meshes of the vessels and, secondly, the visualisation stage which covers the visualisation of these meshes and the presentation in a multiple linked view framework. Figure 3.1 on page 17 shows the data processing pipeline including the results in each case, while Figure 3.2 on page 18 introduces the different components of the user interface.

The goal of the data processing is the extraction of two surface meshes, one representing the inner and one the outer vessel wall border. To achieve this, the OCT data depicting the wall course cross-sectional has to be combined with the MRI data holding the necessary spatial information.

Therefore, in the first step, a 3D structural model of the Circle of Willis is developed from the general medical outline (recall Figure 2.2 on page 7). This 2D scheme and its segment classification were adapted to the 3D positions found in the MRI vessel structure. Then the 3D positions of the segment junctions were measured and transferred to the Circle of Willis scheme. This general 3D vessel model is than adopted to the segment lengths of the Circle from the OCT data, which are obtained through manual measurement. The slice data is investigated at a number of positions along the segment center line and the distance to the inner and to the outer wall is recorded. Based on these measurements, the meshes are calculated and processed in the final step of the data processing by using geometric techniques. Finally, the parameters vessel radius and wall thickness are computed, which are needed for the subsequent visualisation.

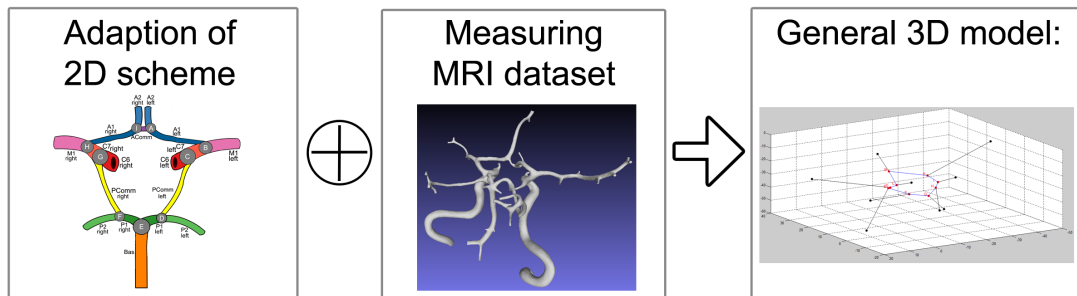
The graphical user interface (GUI) developed during the second stage of implementation can be divided in three components: one view rendering the wall meshes with a color-coding of the parameters, another one displaying an associated OCT slice and, finally, a range of GUI elements providing interaction possibilities for the views.

The software prototype *VesselWallExplorer* is programmed with MATLAB R2013b (The MathWorks, Inc., Natick, Massachusetts, United States, <http://www.mathworks.com/products/matlab>). During the data processing, MeshLab 1.3.3 (open source program, <http://www.meshlab.sourceforge.net>) was employed for mesh processing, while MeVisLab 2.6.1 (MeVis Medical Solutions AG, Bremen, Deutschland, <http://www.mevislab.de>) was used supportive for measuring the OCT dataset.

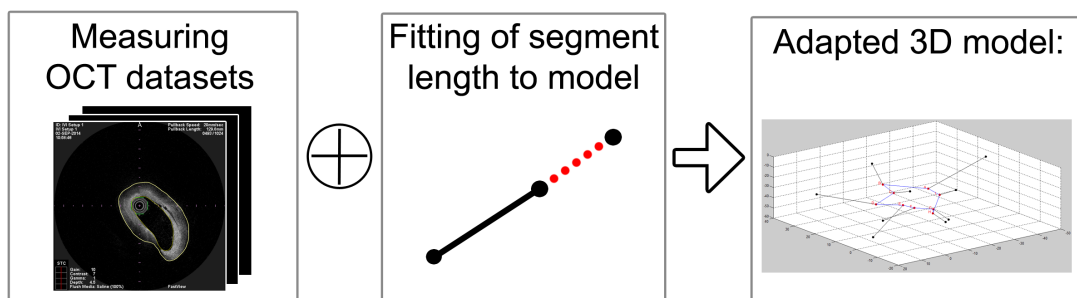
The source code and supplementary datasets are provided at the website <http://www.kristin-baumann.com/vesselWallExplorer>.

# Data Processing

## *Generation of general 3D model*



## *Model adaption to OCT data*



## *Calculation of vessel wall meshes*

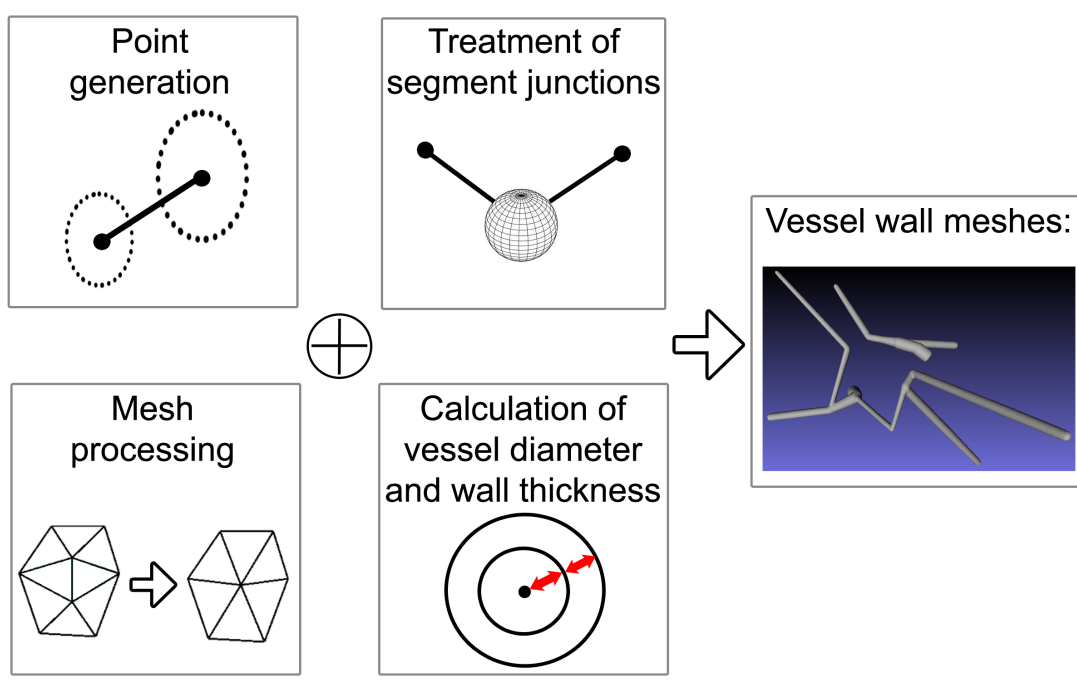


Figure 3.1: Data processing pipeline: from the datasets to the meshes.

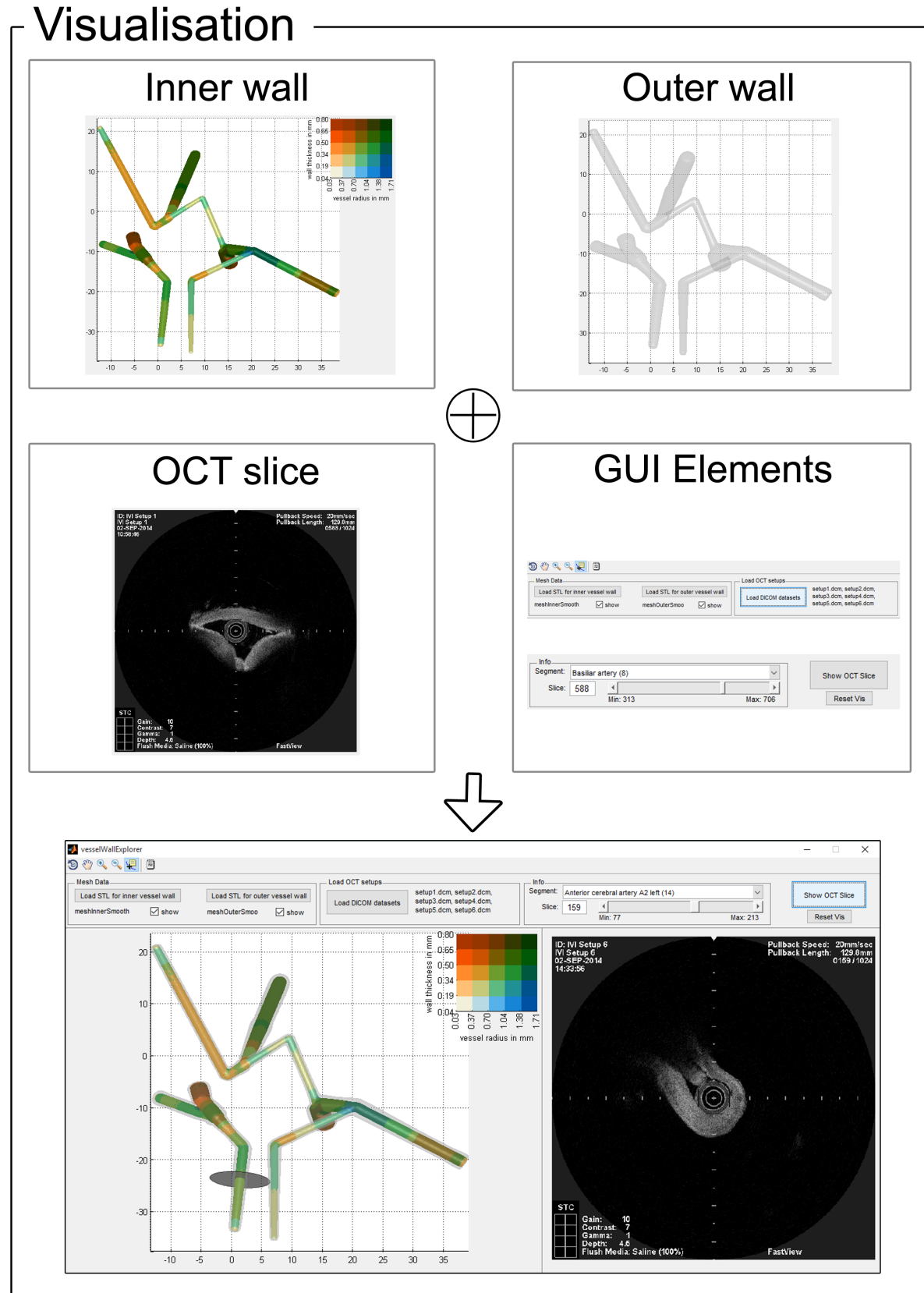


Figure 3.2: Components of the visualisation forming the *VesselWallExplorer*.

## 3.2 Generation of a 3D Circle of Willis Model

In the first step of the data processing (recall Figure 3.1 on page 17), a general 3D model of the Circle of Willis is generated, which can be adapted to the OCT data in the next step. The OCT data itself does not possess spatial information due to the explantation postmortem. To achieve the pursued 3D model, the 2D scheme of the cerebral arterial circle, displayed in Figure 2.2 on page 7, is adjusted to the real conditions of the MRI dataset of the circle. The clinical education MRI dataset with the extracted Circle of Willis surface mesh is employed to extract the spatial positions.

### 3.2.1 Adaption of the 2D Circle of Willis Scheme

The scheme in Figure 2.2 on page 7 is well suited for simplified further processing, but the medical classification of the segments remains as proposed in [HD09]. The location in the Circle of Willis where vessels join will be described as *knots* in the following. For a clear distinction the knots are labelled from *A* to *I* and the segments from 1 to 18, starting at the right ACA running clockwise as shown in Figure 3.4 on page 20.

Inspecting the initial scheme, it is noticeable that all knots link three segment parts except for the connection of the ICA, M1, A1 and PComm on both sides. This position cannot be exactly found in the real MRI dataset, because the A1 and the PComm do not leave the ICA, or respectively the M1 as its extension, at the exactly identical location, but slightly offset as outlined in Figure 3.3. While the generalisation to one point, and thus the joint consideration of segments C6 and C7, is acceptable for a general model demonstrating the structure, this application needs an unambiguous mapping of a point in the vessels to its associated OCT slice. In consequence, the described location is splitted into two knots in the adapted scheme. The PComm joints the ICA first (knots C and G), ending the segment C6 and starting segment C7. The A1 follows shortly after (knots B and H), ending segment C7 and starting M1.

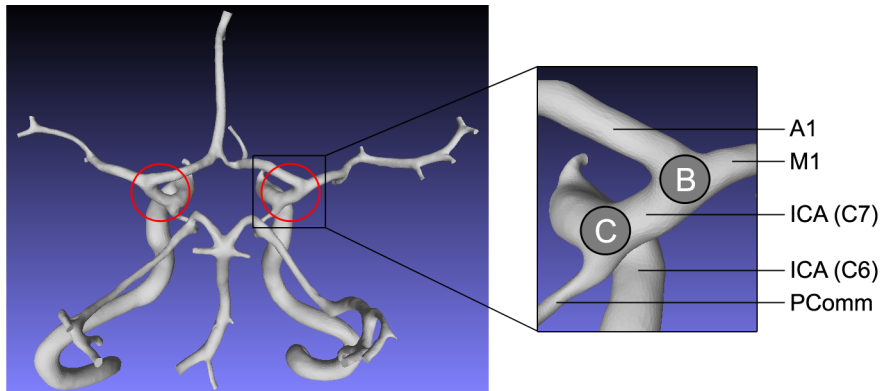


Figure 3.3: Specific adaption of the Circle of Willis scheme at the junctions of the internal carotid artery, marked with red circles. The enlarged view shows the separation in knot B and C in context with the involved arteries in the left part of the arterial circle.

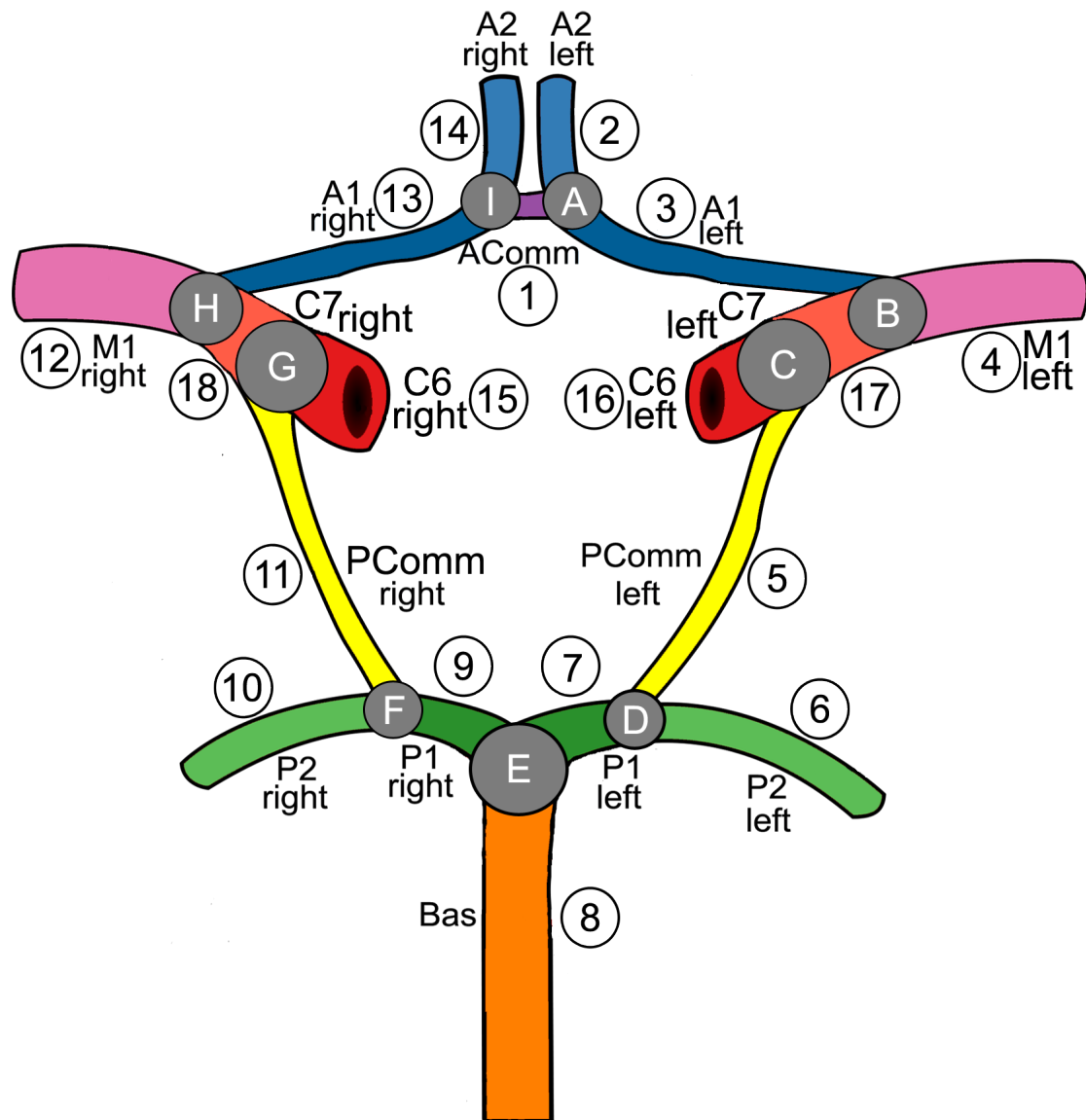


Figure 3.4: Advanced schematic representation of the Circle of Willis with labelled knots and segment numbers (outline based on [Com]).

### 3.2.2 Measuring of 3D Positions from the MRI Dataset

Based on this advanced scheme, the extraction of the spatial positions from the 3D surface mesh of the clinical MRI dataset follows, (recall Figure 2.7 on page 14). Another view of this complex 3D visualisation can be found with Figure A.1 in the appendix.

For each knot of the adapted scheme, the 3D world position is extracted from the surface mesh and is stored. In addition, end points of the individual segments are also determined. Thereby it must be considered that the majority of the cerebral vessels are characterised by high curvature, which, however, is not recorded during the OCT measurement due to the catheter stiffness. It will be disregarded for the moment and the straightened segments are approximated by the 3D position of a knot within the Circle and an according point on the vessel, described as end point. The measurement is carried out based on a point cloud of the extracted surface mesh of the MRI dataset in MATLAB.

As a result of this first step, the measured positions of the vessel knots and the end points of the segments form a general model of the Circle of Willis, see Figure 3.5. The model is prepared for the adaption to the OCT data in the next step.

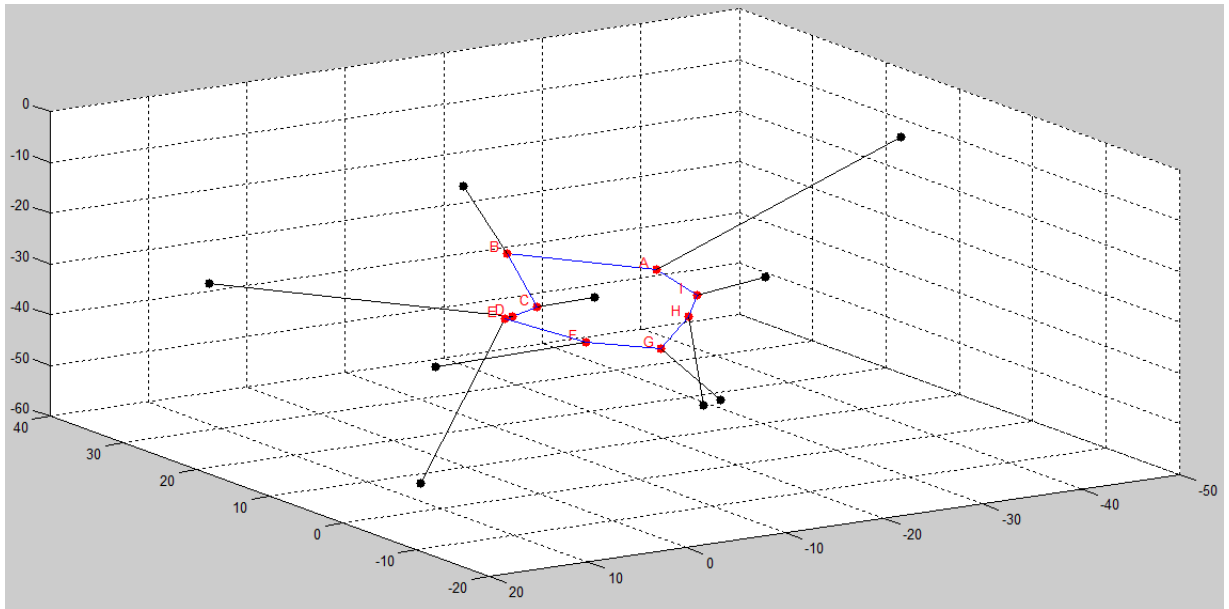


Figure 3.5: General model of the Circle of Willis viewed in MATLAB.

### 3.3 Adaptation of the 3D Circle of Willis Model to OCT Data

This second stage of the data processing deals with the adjustment of the general Circle of Willis model to the given OCT data generating an adapted model, which forms the basis for the calculation of the meshes in the following step. The term adjustment means the fitting of the segment lengths in the model to the lengths measured in the OCT data.

#### 3.3.1 Measuring OCT Datasets

At first, the measurement of the OCT data is carried out. This is not feasible in the way the MRI data was examined before, because each OCT setup comprises a different sequence of segments, see Figure 3.6. For each knot and end point, the according OCT slice is determined by manually scrolling through the 2D OCT image stacks. A vessel junction is indicated, for example, by a vessel cross-section, which shows not a closed, but a rather half-sided open ring.

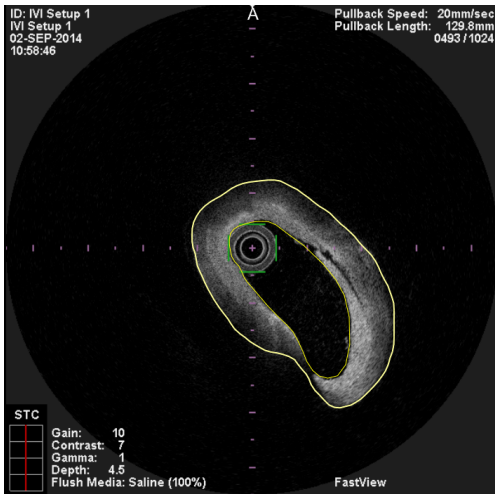


Figure 3.6: Measurement of the OCT slices via the CSOFreehandProcessor module in MeVisLab marking the inner and outer wall border with a yellow contour.

After extracting the OCT slice positions of the segment determining points and up to four arbitrary samples on each segment, the actual measurement of the inner radius (as the distance between vessel center point and inner wall) and the outer radius (as the distance between vessel center point and outer wall) takes place. Since the 3D shape information of the vessels is lost due to the intravascular imaging, the vessel shape has to be approximated, e.g. by cylinders, see Figure 3.7 on page 23. The inner and outer wall are considered separately. This also allows a simplified determination of the required parameters, as there is only one value for each parameter per slice, while in reality a vessel bears at least slightly varying wall thicknesses at its different sides.

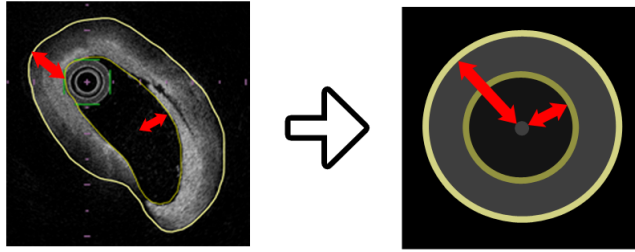


Figure 3.7: Approximation of the vessel shape with circles in 2D and cylinders in 3D, respectively.

The radii can be calculated by applying the formula  $c = 2\pi r$ , where the circumference  $c$  of the inner and outer wall is measured with MeVisLab using the module *CSOFrehand-Processor*. The detection of the contours and their lengths is illustrated in Figure 3.6 on page 22. The final result of these measurements is summarized in the data table Figure A.2 in the appendix. It provides no information for segments with the number 1, 6 and 11, because they were either missing in the specific cerebral arterial circle or too narrow to fit the catheter.

### 3.3.2 Fitting of Segment Lengths to the Model

Now, for each segment, the boundary slices are available. Since the total segment length of a OCT setup is known with 129.8 mm and 1024 slices were acquired, the length of each segment can be computed with a relational equation:

$$\frac{129.8 \text{ mm}}{1024} = \frac{\text{segmentLength}}{\text{endSlice} - \text{startSlice}}.$$

To achieve the model of the Circle of Willis with the previously calculated segment lengths, the positions of the knots and end points have to be modified. In the following, an algorithm is described that moves the knots along their segment line to establish the desired distances.

The input consists of the position of three consecutive knots  $K_1$ ,  $K_2$  and  $K_3$  as well as the intended distance  $d_1$  between  $K_1$  and  $K_2$  and distance  $d_2$  between  $K_2$  and  $K_3$ . Solely the position of the middle point  $K_2$  is altered while the two side knots  $K_1$  and  $K_3$  remain at their place. To find the position  $K_2'$  where the distances to the other two knots are as given, two spheres with centers in  $K_1$  and  $K_3$  and radii  $d_1$  and  $d_2$  are intersected resulting in the plane with an intersecting circle. All points on this circle fulfill the distance conditions to the two outer knots  $K_1$  and  $K_3$ . The point on the circle which is closest to the present location of the original knot  $K_2$  becomes the new position of  $K_2$ .

It follows an explanation of the realisation in three steps:

1. Calculation of the intersecting plane of two spheres
2. Calculation of the center of the intersecting circle
3. Calculation of the radius of the intersecting circle

### Step 1: Calculation of the intersecting plane of two spheres

Equation of a general sphere  $S = (x, y, z)^T$  with center  $M = (x_m, y_m, z_m)^T$  and radius  $r_s$ :

$$(x - x_m)^2 + (y - y_m)^2 + (z - z_m)^2 = r_s^2. \quad (3.1)$$

Identifying the sphere equations of sphere  $S_1$  with center  $K_1 = (x_1, y_1, z_1)^T$  and radius  $d_1$  and sphere  $S_2$  with center  $K_2 = (x_2, y_2, z_2)^T$  and radius  $d_2$  results, as shown in Figure 3.8, in a plane  $P$  in coordinate form:

$$(-2x_1+2x_2) \cdot x + (-2y_1+2y_2) \cdot y + (-2z_1+2z_2) \cdot z = r_1^2 - r_2^2 - x_1^2 + x_2^2 - y_1^2 + y_2^2 - z_1^2 + z_2^2 \quad (3.2)$$

with the normal vector:

$$\vec{n} = \begin{pmatrix} -2x_1 + 2x_2 \\ -2y_1 + 2y_2 \\ -2z_1 + 2z_2 \end{pmatrix} = \begin{pmatrix} a \\ b \\ c \end{pmatrix}. \quad (3.3)$$

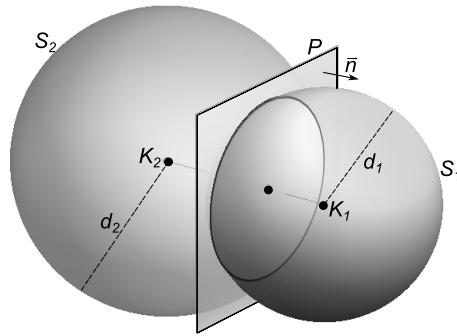


Figure 3.8: Outline of the calculation of the intersecting plane of two spheres.

### Step 2: Calculation of the center of the intersecting circle

The center  $C$  of the intersecting circle is determined by the intersection of plane  $P$  in Eq. 3.2 and the line from one of the sphere centers, e.g.  $K_1$ , running perpendicular to the plane  $P$ , outlined in Figure 3.9.

Line in parameter form equals:

$$C = K_1 + t \cdot \vec{n} = \begin{pmatrix} x_1 \\ y_1 \\ z_1 \end{pmatrix} + t \cdot \begin{pmatrix} a \\ b \\ c \end{pmatrix}. \quad (3.4)$$

Line (Eq. 3.4) entered in plane  $P$  (Eq. 3.2) equals:

$$a(x_1 + a \cdot t) + b(y_1 + b \cdot t) + c(z_1 + c \cdot t) = d. \quad (3.5)$$

Solving Eq. 3.5 for line parameter  $t$  yields:

$$t = \frac{d - a x_1 - b y_1 - c z_1}{a^2 + b^2 + c^2}. \quad (3.6)$$

Replacing Eq. 3.6 for  $t$  in Eq. 3.4 gives center  $C$  of the intersecting circle.

### Step 3: Calculation of the radius of the intersecting circle

As sketched in Figure 3.10, the radius  $r$  of the intersecting circle is calculated using the Theorem of Pythagoras formed by the hypotenuse  $d_1$ , the first cathetus  $r$  and the second cathetus, as the distance between sphere center  $K_1$  and circle center  $C$  using the line from Eq. 3.4. The radius  $r$  is calculated with:

$$d_1^2 = r^2 + (\sqrt{a^2 + b^2 + c^2} \cdot t)^2, \quad (3.7)$$

$$r = \sqrt{d_1^2 - (a^2 + b^2 + c^2) \cdot t}. \quad (3.8)$$

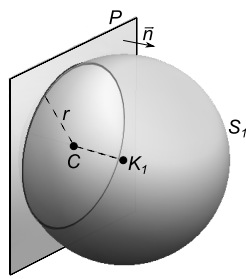


Figure 3.9: Outline of the center calculation of the intersecting circle.

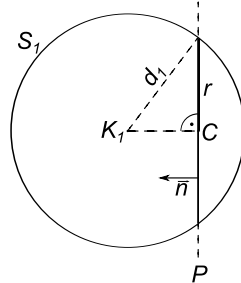


Figure 3.10: Outline of the radius calculation of the intersecting circle.

The previously described algorithm is applied to all sets of three consecutive knots of the Circle of Willis model. The result depends on the order of the inspected sets, because certain knots remain unchanged while others are moved. However, there is no information for the segment lengths for segments 1, 6 and 11 in the present Circle of Willis, as described in the first part of this chapter, hence the Circle of Willis can be considered in two parts. The first part consists of the segments linked by the knots G, H and I; the second part of the segments connected by the knots A, B, C, D, E and F. As a consequence, the knots are processed in the order, thus knots G and I as well as A and F remain at their previous positions whereas knots H as well as B, C, D and E are shifted.

The result of this second realisation step can be seen in Figure 3.11; the adapted model of the Circle of Willis which forms the basis for the mesh calculation in the next step.

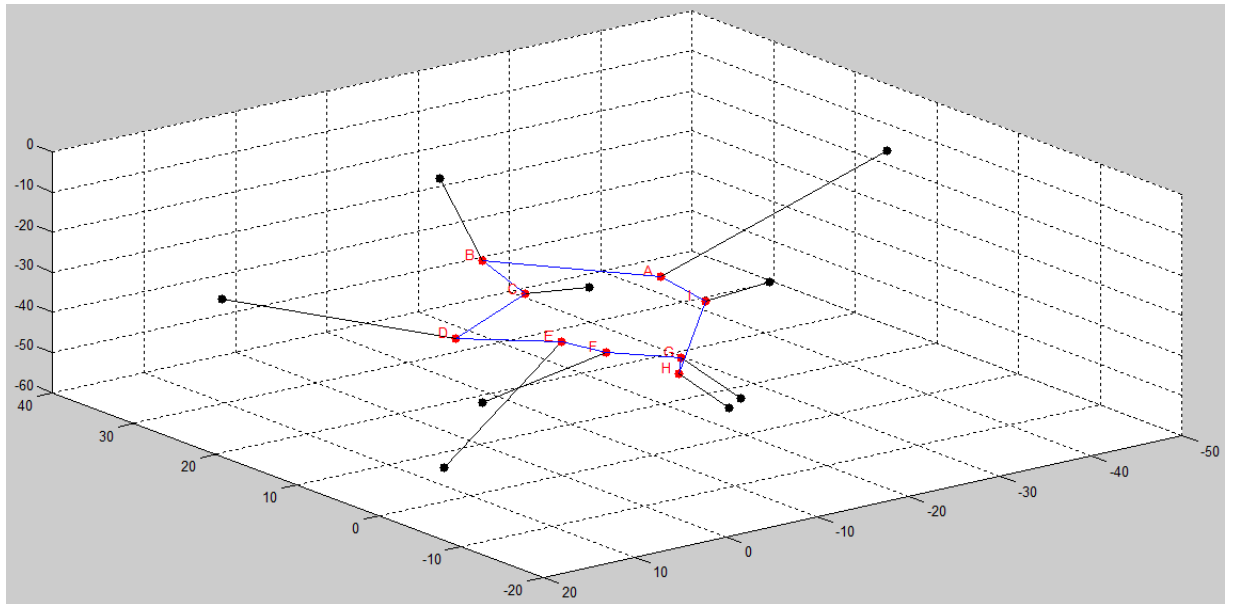


Figure 3.11: Adapted model of the Circle of Willis viewed in MATLAB.

## 3.4 Calculation of 3D Surface Meshes

The last stage of the data processing covers the generation of the 3D surface meshes for the inner and outer wall, based on the adapted model of the Circle of Willis and the previous measurements of the inner and outer radius. This happens in four steps; first, a general calculation of the mesh points is carried out, second, points around the segment knots are handled, third, a 3D triangle surface mesh is extracted and finally, the vessel wall thickness is calculated for the subsequent color-coding.

### 3.4.1 Point Generation

For the mesh generation, a set of points is calculated. Thereby, the inner and outer wall of the vessel are considered separately, because the visualisation in the next stage displays them individually.

As mentioned in Section 3.3, the vessel walls are approximated by cylinders, whereby the segment represents the cylinder center line. Because of the OCT measurements, also described in Section 3.3, it is now possible to assign radii to the cylinders forming the 3D model of the Circle of Willis. For each segment, the underlying data holds the setup number, the start and end knots, the start and end slices as well as two to five sample points with the inner and outer radius. This data table is processed as a CSV file during the implementation. It is attached in Figure A.2 in the appendix. While the radius of the cylinder can be interpolated for points lying on a segment between the measured positions, the knots themselves are treated differently, because the vessel junctions form rather a sphere than overlapping cylinders.

Having the desired cylindrical approximation displayed in Figure 3.7 on page 23 in mind, for each point on a segment line, a 3D circle with the particular radius is calculated and sampled. With this approach, the following algorithm creates an individual array of mesh points for each segment, which is saved in an OBJ file.

1. Sampling of points on a segment between first and last measurement (Omission of the knots).
2. For each sampled point  $p_t$ : calculation of the interpolated inner radius ( $r_{i_t}$  and outer radius  $r_{o_t}$  from the previous and next measurement).
3. For each sample point  $p_t$ : sampling of a 3D circle with the center  $p_t$ , the radius  $r_{i_t}$  or  $r_{o_t}$  and the normal as vector between start and end knot of this segment.

Initially, points on the segment are sampled with a specific sample rate between the start and the end knot of this segment. When such a point  $p_t$  lies between two measurements, which are not at knots, the radii are interpolated with linear interpolation in step two as shown in Figure 3.12.

First, the interpolation parameter  $t$  is calculated between the previous measurement  $m_x$  and next measurement  $m_{x+1}$ :

$$p_t = (1 - t) \cdot m_x + t \cdot m_{x+1}. \quad (3.9)$$

Solving Eq. 3.9 for parameter  $t$  gives:

$$t = \frac{p_t - m_x}{m_{x+1} - m_x}. \quad (3.10)$$

Then the inner and outer radius at point  $p_t$  can be evaluated as:

$$r_{i_t} = (1 - t) \cdot r_{i_x} + t \cdot r_{i_{x+1}}, \quad (3.11)$$

$$r_{o_t} = (1 - t) \cdot r_{o_x} + t \cdot r_{o_{x+1}}. \quad (3.12)$$

Subsequently, the 3D circle can be sampled, as outlined in Figure 3.12.

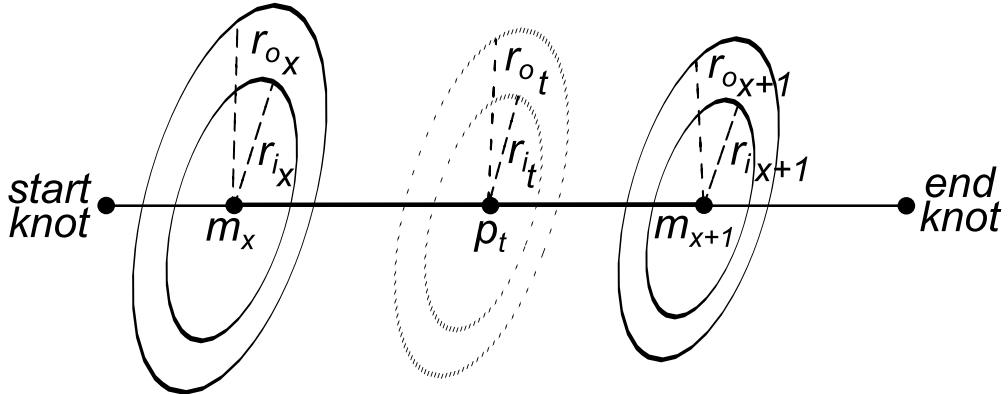


Figure 3.12: Outline of the linear interpolation and sampling of the 3D circle for the mesh generation.

The results of this point generation are 30 point sets, 15 each for the inner and outer surface mesh. These are joined with the vessel junctions into two meshes in the next step.

### 3.4.2 Treatment of Segment Junctions and Mesh Processing

Two methods were carried out for the treatment of vessel junctions. The first approach for generating the mesh points at the knots comprises the application of spheres at these positions, because this shape is closer to the real vessel form at the junctions than overlapping cylinders creating holes and sharp edges. While the knot position obviously describes the center of the sphere, the radius of the sphere has to be chosen as a compromise between the radii of the adjacent segments, which can be quite dissimilar. For the inner wall for example, segment BA has a radius of about 1 mm near knot E, while P1 approximately has a radius of 0.6 mm on the left side and 0.9 mm on the right side.

The result after the mesh building from the point cloud with surface construction algorithms, as described in the following section, can be seen in Figure 3.13. This figure also shows the problem of this approach: If the sphere radius matches the thickness of one segment, it hardly fits with the other adjacent segments. Hence, the segment junctions appear unnaturally prominent and bulky. Another concept has to be carried out to gain more realistic looking results.

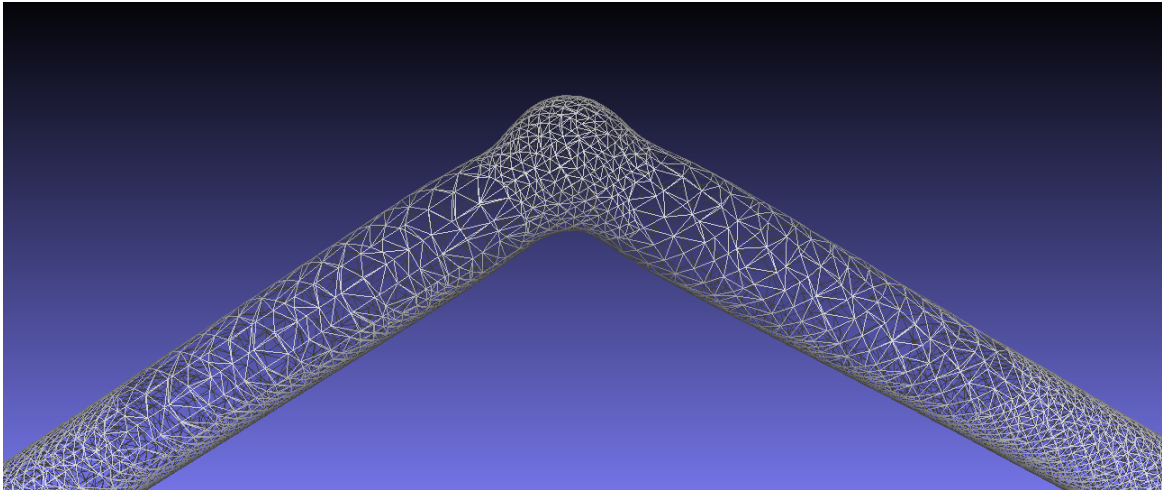


Figure 3.13: First segment junction approach: fitting a sphere to the segment junctions, showing segment 2 and 3 connected by knot A, viewed in MeshLab.

The second approach does not aim to perfectly place the mesh points in the first place, but deals with the precise usage of a surface reconstruction algorithm to create a hole-free and smooth surface. To generate the points, the algorithm with the sampling of a 3D circle described in the previous step on page 27 is applied with a minor adaption. For each segment end, the circle points are not only sampled between the last measurement and the knot itself, but also on the slightly extended segment beyond the knot. This causes a larger overlapping of adjacent segments, as shown in Figure 3.14, and with that smaller holes at the vessel junctions, which can be fixed easier by a surface reconstruction algorithm from the point cloud.

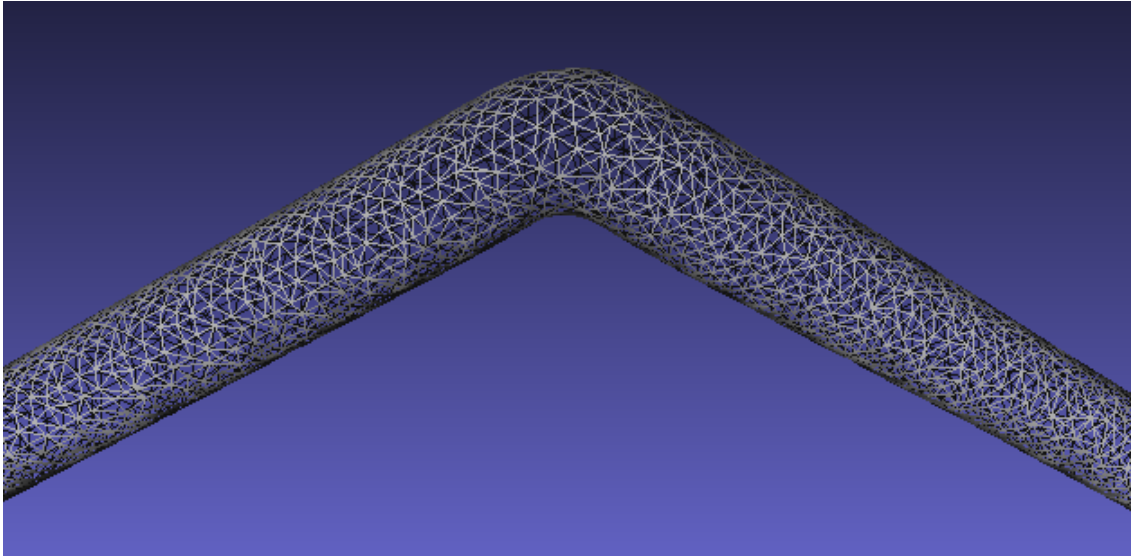


Figure 3.14: Second segment junction approach: overlapping cylinders linked by using the Poisson Surface Reconstruction algorithm viewed in MeshLab (showing segment 2 and 3, connected by knot A).

After carrying out simple reconstruction algorithms, like Ball Pivoting, that yield in unsatisfactory, holey outputs, the Poisson Surface Generation algorithm introduced by Kazhdan et.al. in [KBH06] produces the most realistic meshes when using an appropriate parameter selection. The algorithm is implemented in MeshLab. The method requires a point set with oriented normals as input. To achieve this, the normals for each point in the previously composed point cloud are computed using the tool *Compute normals for point sets* in MeshLab, which evaluates the weighted product of the k-nearest neighbors, in this case with  $k = 20$ . It has to be observed that a flipping might be necessary in order that the normals point outward, away from the segment middle line.

Now, the isosurface can be approximated from the normal field of an indicator function, which is zero everywhere except for areas enclosed by the surface. This function is derived from a gradient resulting from the oriented points. The extraction of the isosurface and the triangles forming the mesh is then performed by applying the *Marching Cubes Algorithm*, which constructs an octree data structure for the representation of the surface. A detailed description of the Poisson Surface Reconstruction algorithm can be found with illustrative images in [TUBFM].

Several parameters have to be selected for this algorithm in MeshLab, which strongly affect the outcome. The most important one is the *octree depth*, influencing the precision of the reconstruction. A higher depth leads, however, to a longer processing time. Furthermore, the *samples per node* indicates the minimum number of sample points within an octree node, adapting the octree construction to the sampling density and thereby the level of detail. Because the data in the present case can be considered as noise-free, the parameters are chosen as follows:  $depth = 12$  and  $samplesPerNode = 1$ .

Since the meshes are generated with a high level of detail and thus are very memory-intensive, they have to be post-processed to be utilized in a convenient way in the framework described in the following section. The mesh decimation is performed with the help of MeshLab's *Cleaning and Repairing* tool *Merge close vertices*, which merges all vertices together which are closer than a specific threshold:  $mergingDistance = 0.08mm$ . The resulting mesh for the inner vessel wall border, shown in Figure 3.15, consists of about 206,000 vertices and the outer one of about 233,000 vertices.

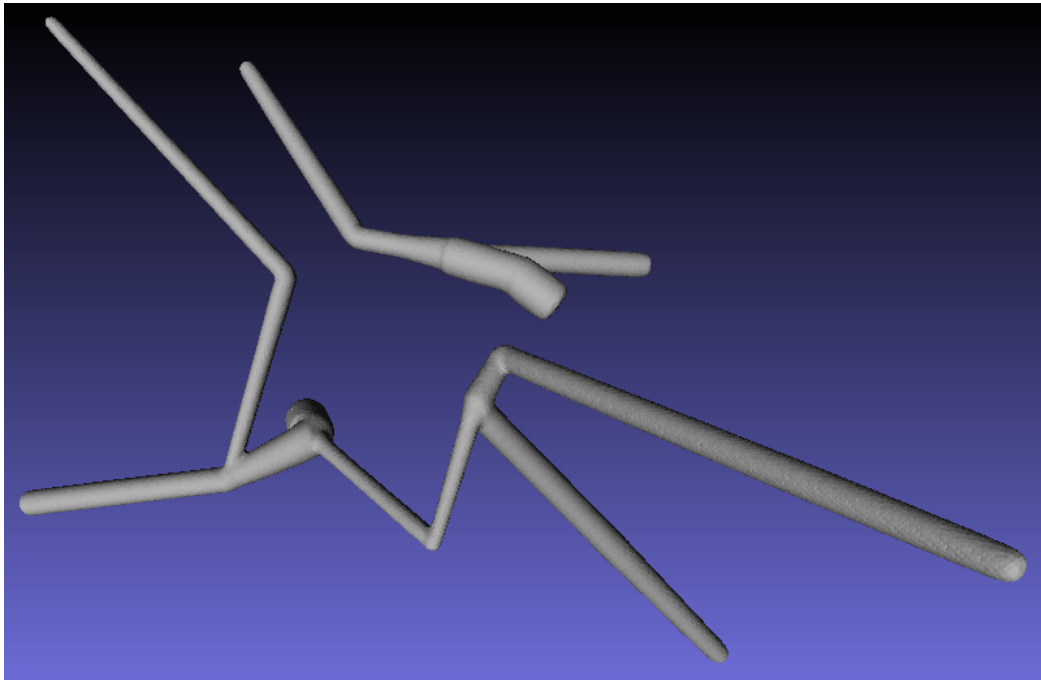


Figure 3.15: Post-processed mesh of the inner vessel wall border, viewed in MeshLab.

### 3.4.3 Calculation of Vessel Diameter and Wall Thickness

To complete the visualisation in a multiple linked view framework, the two parameters *vessel radius* and *vessel wall thickness*, which should be mapped on the meshes, have to be calculated. The calculations are done for each vertex in both meshes, based on the stored information for the single segments (recall Section 3.3).

The *vessel radius* is calculated for the mesh vertices of the inner surface mesh as the distance to the closest point on the corresponding segment. Since a vertex is not associated with the segment from the Circle of Willis model forming this vessel, this connection has to be established in the first place. Then the closest point to the vertex, which defines the vessel radius can be calculated. This process is done using Euclidean distances in two approaches described in the following.

The first approach, outlined in Figure 3.16, separates the segment association from the nearest point determination. The related segment of a mesh vertex is identified by choosing the segment, where the distance between the vertex and the start and end knot of this segment, is smallest. Then, the vertex is 3D projected on the selected segment line with the usage of the dot product. This concept provides appealing results for short segments, but the segment matching fails for long segments like the BA, because other start or end knots might be closer in 3D than the actual ones. Therefore, a further approach has to be undertaken.

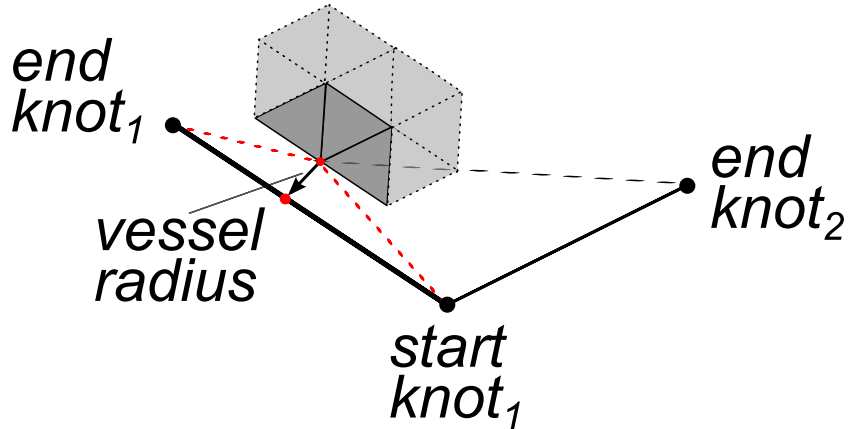


Figure 3.16: First approach of calculating the vessel radius using 3D point projection.

The second and final approach, shown in Figure 3.17 on page 33, combines the two steps in one. All segment lines are sampled by using linear interpolation between the start and end knot like in Eq. 3.9 on page 28. The sampled point with the shortest distance to the mesh vertex is used for the distance calculation resulting in the vessel radius. This approach is clearly more computationally intensive, but the results with a sampling rate of 0.05 are significantly more precise.

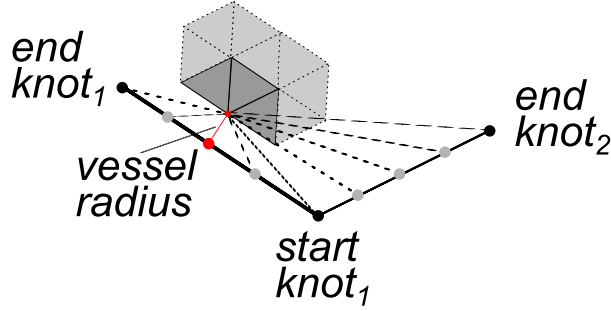


Figure 3.17: Second approach of calculating the vessel radius using sampling of the segment.

The *vessel wall thickness* for a vertex of the 3D triangle surface mesh can be defined as the distance to the closest vertex in the other mesh, because the vessel form is approximated as a straight cylinder, shown in Figure 3.7 on page 23, and there are only slight changes of the parameters within a segment. Therefore, it is necessary to establish a connection between the two meshes.

While finding the two closest points of the meshes, the mesh sizes of about 200,000 vertices have to be considered. A simple comparison of all vertices of one mesh with all vertices of the other mesh is due to an enormous computation time not possible and therefore, the comparisons have to be reduced. This is achieved by dividing the vertices in each mesh in buckets based on their location on the segment.

This classification is done again with linear interpolation and a distance comparison. For each vertex, the matched segment is sampled with a rate of 0.1 and the sampled point with the closest distance indicates the bucket. This classification is saved in MATLAB as a cell-in-cell array consisting of 18 outer cells, one for each segment. Each of these cells holds 10 buckets, due to the sampling rate of 0.1, and each bucket lists the indices of the vertices in this bucket.

Afterwards, the wall thickness is calculated for each vertex by selecting the smallest distance of the vertex to the points in the according bucket of the other mesh. The result of the three previously explained data processing steps are two surface meshes approximating the image data from the OCT setups of the Circle of Willis, as well as the calculated parameters vessel radius and vessel wall thickness, ready to be visualised in the next step. The mesh of the inner vessel wall border can be seen in Figure 3.15 on page 31, while the outer vessel wall border is displayed in Figure A.3 in the appendix.

### 3.5 Multiple Linked View Framework

After finishing the calculations to gain the vessel surface meshes and the according parameters, the Circle of Willis can now be interactively displayed in a graphical user interface (GUI). On the one hand, it allows the user to simultaneously view the vessel radius and wall thickness of the complete Circle, on the other hand, a detailed investigation of the vessel structure is possible by means of a multiple linked view framework showing the OCT slice for a specific 3D point on the vessel surface mesh. The complete GUI is depicted in Figure 3.18 on page 35. Its components and their functionality are explained in the following.

The interface consists of three parts: the mesh visualisation view on the left showing the color-coded inner and outer vessel border, the display of the OCT slice on the right and a control bar at the top. This subdivision is performed in the visualisation overview in Figure 3.2 on page 18.

The most important feature is the **mesh view**, because it shows the vessel surface meshes with a bivariate color-coding of the two parameters as well as the according legend. The 3D view can be manipulated with the help of the pan, zoom and rotate tools located in the menu bar, provided by MATLAB.

The display on its right shows a **slice of an OCT setup** of the Circle of Willis. The user can examine the setup by operating the slider in the control bar to change the slice number. Moreover, the info panel indicates the segment name and the current slice number.

The **GUI control bar** contains, next to the already mentioned OCT info panel with the slider, fields to load the mesh and OCT setup files as well as buttons to show the OCT slice and to reset the mesh visualisation.

The mesh and the OCT slice view are connected as a multiple linked view framework, so that the user can analyze the vessel cross-section in the OCT image for a previously selected point in the vessel structure. The particular operation procedure is described below.

After loading the surface, the user can view and hide the vessel meshes in 3D and select a vertex in the mesh by using the data cursor tool from the menu bar. A successful selection is indicated by showing the 3D coordinates of the point. By pressing the *Show OCT slice* button, the previously black display on the right is then populated with the OCT slice of the vessel at the picked vessel point, which is highlighted in the visualisation with a grey sectional circle. Now both views are linked. While exploring the OCT setup by scrolling through the slices, as mentioned in the paragraphs beforehand, or entering a precise slice number, the position of this grey glyph updates correspondingly in the mesh visualisation. The data in the OCT info panel refreshes as well. Another point can then be selected in the vessel structure and the procedure repeats.

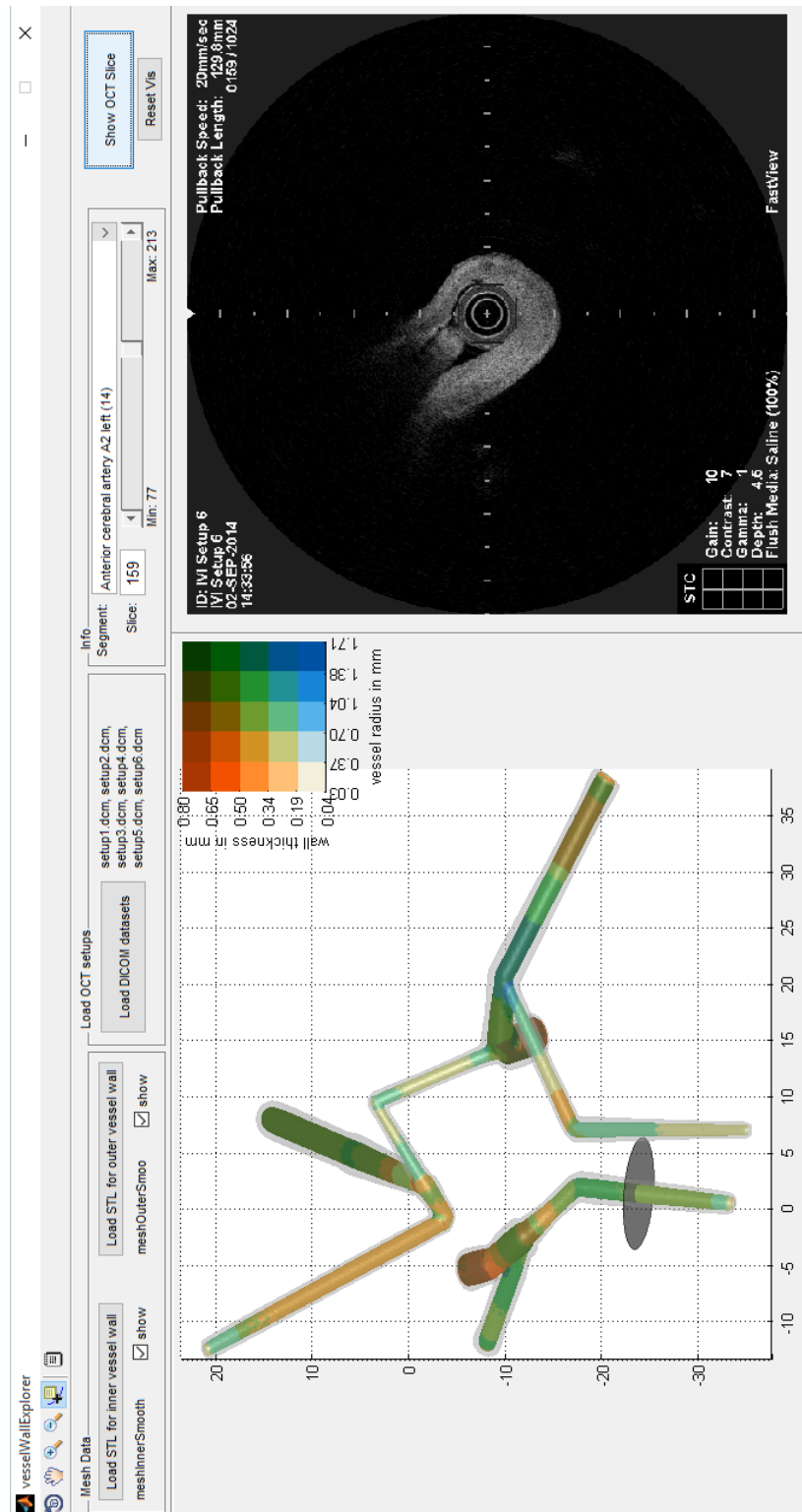


Figure 3.18: Multiple linked view framework *VesselWallExplorer* displaying the vessel meshes and the according OCT slice, implemented with MATLAB.

### 3.5.1 Loading of the Surface Meshes and the OCT Image Data

As a prerequisite for the exploration of the 3D and 2D image data, the datasets have to be loaded as fast as possible. The loading buttons can be found in the control bar, shown in Figure 3.19.

For the GUI, all six OCT setups files, each consisting of 1024 slices with a resolution of 600 x 600 pixels, are needed. After converting them to .dcm files, each setup is still large with about 1 GB, thus the user gets feedback via a loading bar. The reading in the GUI is then performed with the MATLAB function *dicomread*.

The meshes were post-processed with mesh decimation algorithms, as described in Section 3.4.2 on page 31. Therefore the file size and in consequence the loading time can only be reduced by changing the storage format. So far the meshes persist as .obj files with sizes of about 8.5 MB for the inner mesh and 10 MB for outer mesh. By saving them as binary .stl files with MeshLab the file sizes can be reduced to approximately 3 MB for both. The reading in the GUI is then carried out with the *stlread* function from [EW11] which reads the .stl meshes into vertex and face matrices.

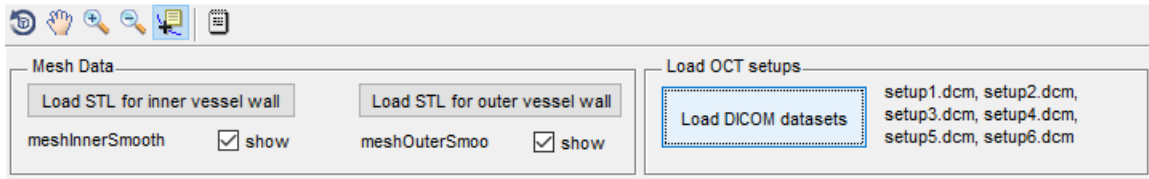


Figure 3.19: GUI component: loading of the surface meshes and the OCT image data.

### 3.5.2 Color-coded 3D Visualisation of the Triangle Surface Meshes

The recently mentioned vertex and face matrices form the basis for the rendering of the Circle of Willis surface meshes, because they are the input of the MATLAB *patch* function, which draws the polygons into the left 3D view. The desired color-coding of the two parameters is then enabled by additionally specifying the attribute *FaceVertexCData* as three-column matrix with the number of mesh vertices as row number. Each row states the color of the indexed vertex with an RGB triplet in the range of [0,1]. The color of the face is then bilinear interpolated from the vertex color by setting the attribute *FaceColor* to *interp*. The same Gouraud based approach is implemented for the calculation of the lighting, as the light at the vertices is interpolated to determine the light across the face.

After the general color-mapping implementation, the mapping of the parameter values per vertex to a color is the next step. As described in Section 3.4.3 on page 32, the vessel radius and the wall thickness are present for each vertex on both meshes. A meaningful mapping has to guarantee that the simultaneous display of the parameters allows a clear and distinctive investigation of the values of a single parameter. Two approaches for the color mapping were developed for this thesis.

In the first approach, the vessel radius is mapped on the triangles of the surface mesh of the inner vessel wall border and the parameter values for the wall thickness on the outer mesh. The latter is rendered with a certain level of transparency such that the inner structure is still perceptible. Both parameters are mapped with a single scale, thus one color represents one value in both parameter ranges. With MATLAB's default color scale, the rainbow scale, shades of blue represent low distances, red shades distances near the maximum and green and yellow tones the values in between. The scale runs from 0 mm to 1.8 mm, which is the maximum of the combined value ranges.

The result of this mapping, displayed in Figure 3.20, does not completely fulfill the previously set goal, because the color interference of inner and outer mesh and the necessary transparency of the outer mesh make it difficult for the user to observe the single parameters. Another problem is the dissimilar value range. The vessel radius reaches values up to 1.8 mm, while the wall thickness touches just about 0.8 mm. Therefore the thickness is mostly represented by shades of blue and variations in it are hard to spot. Even changes of the color scale, e.g. to a continuously single hue gradient, do not noticeably improve these circumstances.

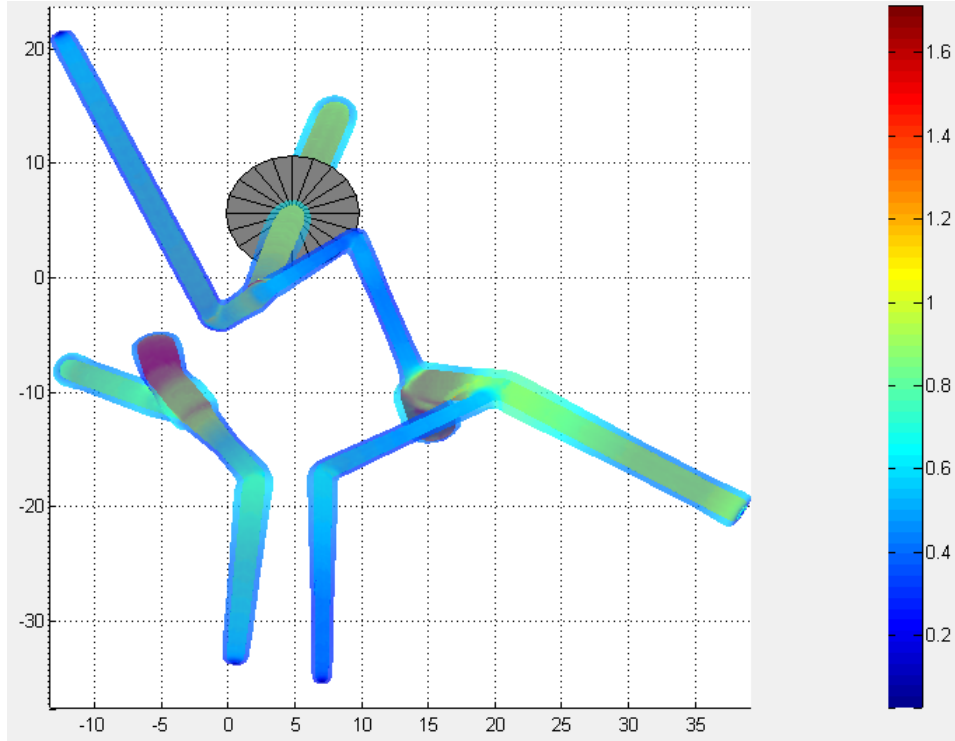


Figure 3.20: GUI component: first approach of the color-coded meshes showing the vessel radius on the inner and the wall thickness on the outer surface mesh.

To overcome the color blending problems, the second approach comprises a bivariate mapping of the parameters on the inner mesh only, while the outer mesh is rendered slightly transparent in gray to provide context information. A color then represents two parameters: a certain range for the vessel radius and at the same time a possibly different range for the wall thickness.

The underlying color matrix, as included in Figure 3.21, arises from the multiplicative overlaying of two single hue gradients. These gradients are chosen in a way that the individual colors in the resulting matrix are easily to distinguish. In this case, the vessel radius is depicted by shades of blue on the x-axis and the thickness by orange tones on the y-axis. This results in a green diagonal, which sums it up to roughly three color areas, each one representing one combination of parameter values. Light colors signal low values, while strongly saturated ones indicate high values for both parameters. Dark orange maps thereby a high wall thickness but a low vessel radius, dark blue for the reverse and dark green is assigned to areas with increased vessel wall thickness and vessel radius.

To avoid high visual complexity and to support visual clustering, each axis is divided into 5 buckets. Therefore, the number of colors the user has to differentiate is limited to 25. Furthermore, fading in and out of the individual meshes is possible by a checkbox next to the loading buttons, making the color appearance even more obvious while allowing the user to investigate the context. Another advantage of this second approach is the possibility to directly read the correlation of the parameters when watching out for the green segment parts, visible in Figure 3.21.

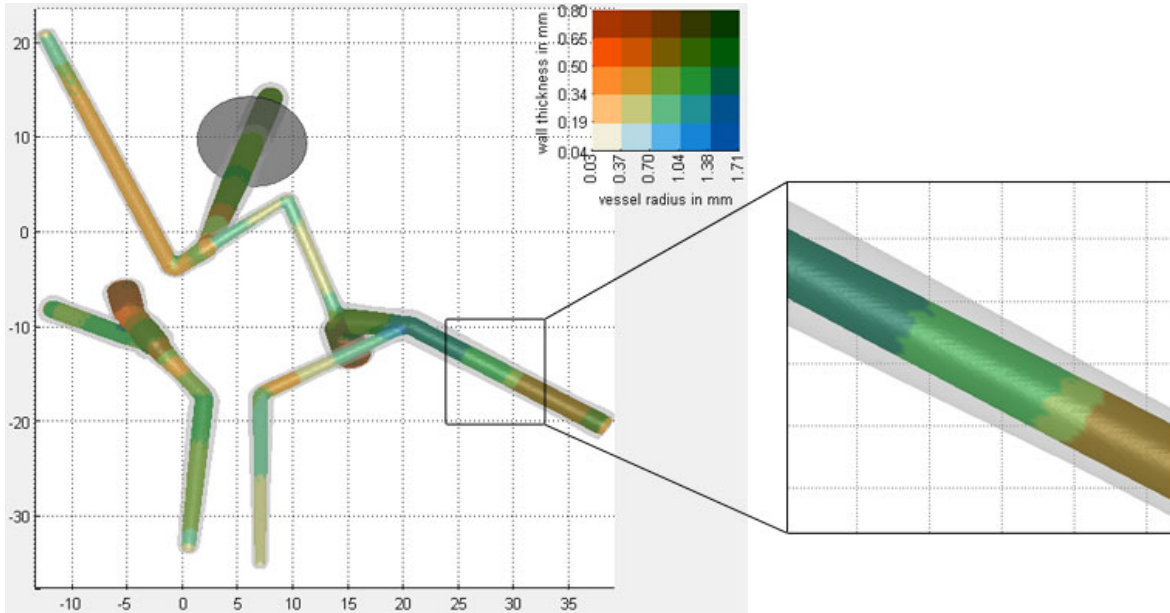


Figure 3.21: GUI component: color coded visualisation of the inner vessel wall border and the transparent outer vessel wall border.

### 3.5.3 Linking the 3D Surface Mesh View with the 2D OCT Slice View

While the colored mesh rendering allows a good general overview of the parameter distribution, a detailed investigation of the vessel wall is only possible in combination with the study of the particular OCT slices. This enables an inspection of the construction of the vessel wall and the characteristic of the different wall layers. In the process, pathologic wall thickening and other indications of cerebral artery disease as explained in Chapter 2 can be detected by viewing the cross-sections.

Furthermore, the mesh is based on the approximation of cylinders; in reality the wall thickness might not be identical on all sides. Viewing the actual shape might bring new insights. For example, Figure 3.22 shows a vessel cross-section in the central part of the BA, which features a small vessel radius, as the catheter just fits through. The medium wall thickness remains mostly the same, however, the vessel ellipse is interrupted on the lower right side, because at this point a vessel branching exists. Therefore, the exact determination of the vessel wall boundaries is not possible.

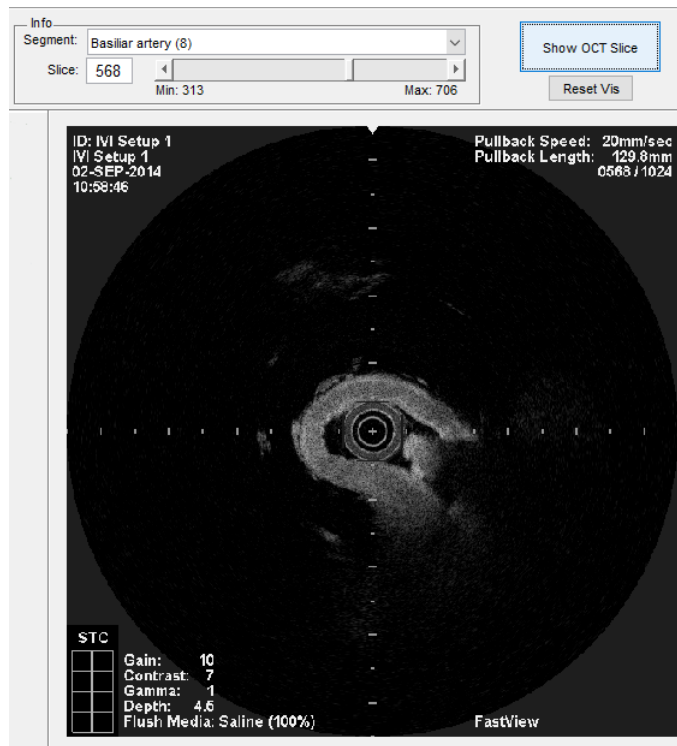


Figure 3.22: GUI component: 2D OCT slice views with interaction elements.

The linking of the two views during the exploration is based on the mutual matching between the 3D position of a vertex of the mesh and the corresponding slice number in the OCT setup, which is presented in the following paragraphs.

First, the 3D position is determined with MATLAB's *data cursor mode* feature after a click in the surface mesh view. For an easier and faster processing, the closest point on the segment center line is derived by partly using the algorithm used for the parameter calculation in Section 3.4.3 on page 32 which applies sampling of the segments and determining the point with the shortest distance. The selected point i.e., the vertex of the surface mesh, is then marked with a glyph for user's reference. This glyph, visible in Figure 3.18 on page 35, consists of a slightly transparent, grey circle plane oriented perpendicular to the segment line. Hence, the same calculation steps are carried out as for calculation of the 3D circle (recall Figure 3.12) but with an increased radius of 5mm (2.5x of the largest outer radius), which makes the glyph clearly visible, as shown in Figure 3.23.

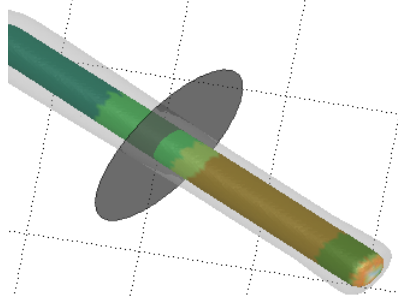


Figure 3.23: GUI component: glyph highlighting the current slice position.

After that, the slice number  $s$  in the OCT setup matching the 3D location  $pos$  of the point in the mesh has to be identified. Here, an already introduced method, more precisely linear interpolation on the segment like in Eq. 3.9 and Eq. 3.10 on page 28, is suitable, because for each segment, the 3D positions  $k_1$  and  $k_2$  as well as the slice numbers  $s_1$  and  $s_2$  of the segment start and end knot are known. The interpolation parameter  $t$  is calculated from the interpolation of the knot positions and then entered in the linear interpolation equation of the slice numbers:

$$t = \frac{pos - k_1}{k_2 - k_1}. \quad (3.13)$$

$$s = (1 - t) \cdot s_1 + t \cdot s_2. \quad (3.14)$$

The slice  $s$  of the corresponding OCT setup can be viewed in the right view and simultaneously manipulated by the slider, which then triggers an update of the glyph position in the mesh view accordingly. To recalculate the position of the glyph, the same method as described above is applied. The interpolation starts with the new slice number and is then entered in the knot position interpolation.

This linking of the 3D surface mesh view with the 2D OCT slice view completes the multiple linked view framework to display the Circle of Willis with focus on the vessel wall. Feasible improvements and criticisms are discussed in the following chapter.

## 4. Discussion

The presented software supports medical experts, who want to examine the vessel wall with possible pathological manifestations of cerebral diseases located in the Circle of Willis. Therefore, the color-coded visualisation allowing a precise observation of the relation of the vessel radius and the wall thickness was created. By linking with the original OCT image data, it enables a selective consideration of locations, that stick out in the overview visualisation. For example, the OCT slice can be easily examined for a position colored in dark orange in the midst of an otherwise mostly greenish vessel, representing a narrowed vessel part, which could possibly indicate arteriosclerosis leading to a stroke. Similar to this, a sudden less saturated spot might signal a weakened, thin wall, which is vulnerable to a rupture causing a hemorrhage.

In the present cerebral arterial circle, shown with legend in Figure 3.21 on page 38, the radius and wall thickness seem to directly correlate, as the green colors on the diagonal line of the bivariate mapping are most present. This fact is also underpinned in the 3D histogram in Figure 4.1 on page 42, which shows significantly higher values for the described parameter ranges. As expected, the supplying arteries BA and ICA are thicker and wider than the remaining vessels, whereby the BA has an overall bigger radius with values between 1.04 and 1.38mm but a slightly smaller wall thickness of 0.5 to 0.65mm compared to the ICA with a radius of 0.7 to 1.04mm and a wall thickness of 0.65 to 0.8mm. In contrast to this, the right PComm, as the sole vessel part linking the supplying with the outbounding arteries (since the left artery is missing due to the patient-individual anatomy), is one of the smallest and thinnest artery with a radius of 0.37 to 0.7mm and a wall thickness of 0.19 to 0.34mm.

Since the *in vivo* use of OCT imaging is not authorised for cerebral vessels yet, the data from specimens explanted post mortem used in this work is quite rare. Due to the novelty of the presented medical application, a ground truth in form of other software implementations is not available. For a detailed evaluation of the medical relevance, a user study with medical experts has to follow.

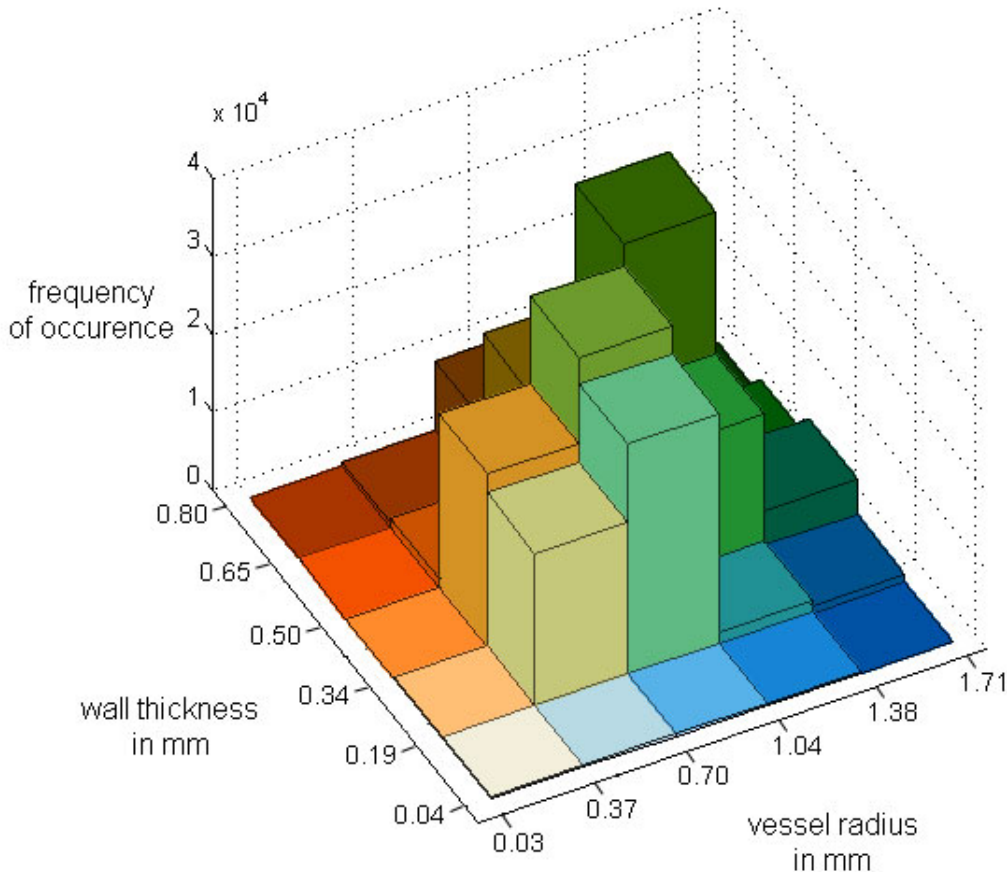


Figure 4.1: Bivariate histogram showing the parameter distribution of the vessel radius and the vessel wall thickness in the inspected Circle of Willis, generated with MATLAB's *hist3* command  
 (see Section 3.5.2 for detailed explanation of the color-coding).

When evaluating the software prototype by its aspects as an interactive system, the following considerations are noteworthy. Overall, the application consists of a clear interface with three distinctive components. The step-by-step operation procedure with the loading, the point selection and the manipulating of the OCT slice is clearly prescribed for the user, because only available control elements are active and clickable, while the others are inactive. Furthermore, the user receives feedback like loading bars and error messages.

This software prototype started from the scratch and no similar application exists so far. Therefore, several improvements are possible, that could address the following points of criticism in the future.

The most striking issue is the approximation of the vessels with straight cylinders, which causes a noticeable difference between the slightly abstract visualisation and the strongly curved vessel structure in the real human body. So far, the 3D information of the cerebral circle, which is not available in the intravascular imaging of the explanted specimen, is gained by a manual sampling of an additional MRI. The resulting 3D locations are matched with the according knot positions in the OCT data of the cerebral circle. Subsequently, the 3D points are combined to the model of the Circle of Willis, as they approximate the segment middle lines with a start and end point as well as several sample points in between. Future work could include an algorithmic approach to gain the segment middle lines as well as the application of more advanced geometrical shapes like splines for the center line approximation or, in consequence, curved cylinders for the vessel form.

Furthermore, the measurement of the OCT slices can be improved, as the determination of the contours of the inner and outer wall border is manually carried out as well. Up to four measurements are performed per vessel, depending on the vessel length. An automatic extraction would lead to a greater precision of the visualisation due to a significantly higher sample rate and therefore less deviation caused by interpolating the parameters for locations between the measuring points. This is conceivable by using image processing methods like *active contour models* [KWT88] with a closed circle as starting spline or a variant of *balloon force*, because the 2D image would feature a sufficiently high gradient at the inner and outer wall borders.

For an application in clinical environment, the software would need more efficient processing of the data. This includes a reduction of manual steps as mentioned in the issue before. For a better user experience, the loading time of the OCT setups as DICOM files has to be decreased. Moreover, the calculations should be feasible in real-time, e.g. by distributing the computations on multiple threads.



## 5. Summary

In this thesis, a multiple linked view framework including a visualisation of optical coherence image data of the cerebral arterial circle was introduced in order to enable its exploration and the evaluation of the cerebral artery wall.

The process started with the raw OCT data and then described the transformation into 3D meshes of the inner and outer vessel wall border by creating a general model of the Circle of Willis using an MRI scan. Two meaningful parameters, the vessel radius and the vessel wall thickness, had been selected and were color-coded on the meshes with a single bivariate mapping. The resulting visualisation is displayed in a graphical user interface, in which it is linked to the initial OCT data. This allows the user to select an interesting point in the 3D visualisation which then triggers the display of the according slice in the dataset, and vice versa.

This work aims to improve the diagnosis and risk analysis of cerebral diseases in the Circle of Willis by using intravascular imaging. A sufficient assessment of the disorders is important for the indication of therapy, since these diseases, e.g., cerebral infarction, hemorrhages or cerebral aneurysms, have a relatively high incidence, a sudden occurrence and a mostly fatal outcome. The OCT imaging method allows the acquisition of the vessel wall, including its layers and borders, with a superior spatial resolution. The medical application evolving from this thesis allows the display of the vessel wall characteristics in context with the vessel structure itself, because the wall is subject to pathological changes in most cerebral diseases like in case of arteriosclerosis.

Next to this improved assessment of serious diseases, this work also clearly demonstrates the important role of meaningful visualisations of medical image data, as it enables medical experts to explore 6.144 OCT slices (6 OCT setups à 1024 slices) in just one glance. As soon as the OCT imaging is authorised for in vivo use, the amount of data will increase and the described processing of raw OCT image data to meaningful visualisations will be even more necessary.



## A. Appendix

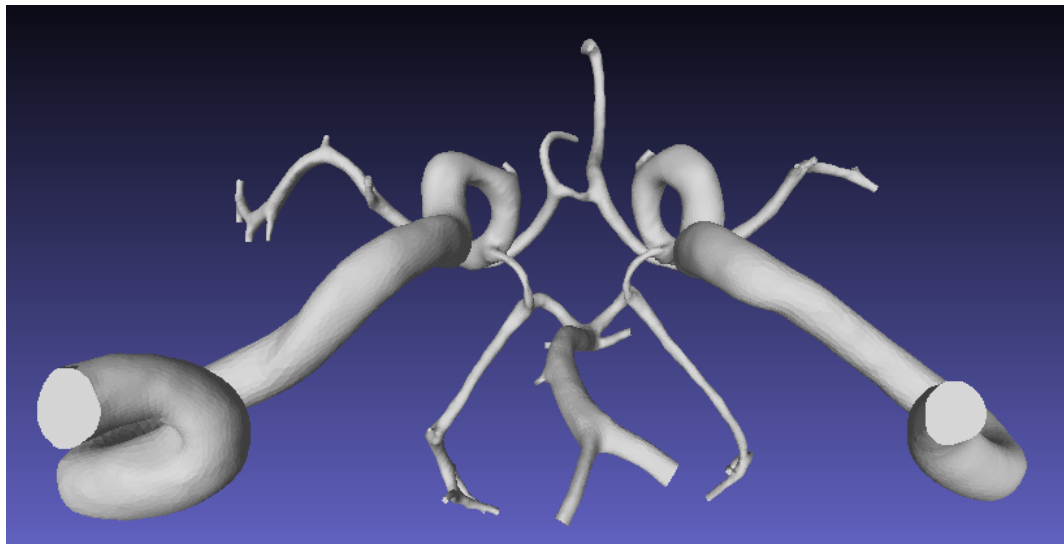


Figure A.1: View from below of the Circle of Willis reconstructed from the MRI data displayed in MeshLab.

Segment	Setup	Length Setup (mm)	Start Slice	End Slice	Start Knot	End Knot	M1 Slice	M1 inner (mm)	M1 outer (mm)
1	0	0	0	0	0	0	0	0.000	0.000
2	4	129.8	59	241	A2r	A	59	0.501	0.832
3	4	129.8	241	365	A	B	252	0.755	1.071
4	2	129.8	725	892	B	M1r	744	0.934	1.324
4	3	65	259	602	B	M1r	294	0.954	1.732
4	4	129.8	365	525	B	M1r	381	0.906	1.416
5	2	129.8	563	672	D	C	580	0.645	0.995
6	0	129.8	0	0	0	0	0	0.000	0.000
7	2	129.8	492	563	E	D	508	0.631	0.976
8	1	129.8	313	706	E	Bas	355	1.006	1.391
	2	129.8	67	492	Bas	E	67	1.027	1.637
9	1	129.8	281	313	F	E	288	0.859	1.180
10	1	129.8	53	281	P2l	F	53	0.673	1.057
11	0	129.8	0	0	0	0	0	0.000	0.000
12	5	65	59	310	M1l	H	59	0.980	1.663
13	6	129.8	213	344	I	H	225	0.817	1.265
14	6	129.8	77	213	A2l	I	77	0.691	1.062
15	5	65	388	428	G	C6l	400	1.509	1.922
15	6	129.8	360	386	G	C6l	363	1.438	1.918
16	3	65	109	130	C6r	C	109	1.901	2.501
17	2	129.8	672	725	C	B	705	1.163	1.662
17	3	65	146	259	C	B	162	1.381	2.001
18	5	65	310	388	H	G	349	1.412	2.039

Segment	M2 Slice	M2 inner (mm)	M2 outer (mm)	M3 Slice	M3 inner (mm)	M3 outer (mm)	M4 Slice	M4 inner (mm)	M4 outer (mm)
1	0	0.000	0.000	0	0.000	0.000	0	0.000	0.000
2	120	0.582	0.862	230	0.713	1.200	0	0.000	0.000
3	292	0.663	0.961	346	0.608	1.060	0	0.000	0.000
4	827	1.103	1.434	892	1.129	1.651	0	0.000	0.000
4	453	1.042	1.491	549	1.052	1.504	602	1.123	1.785
4	457	1.199	1.486	525	1.236	1.664	0	0.000	0.000
5	604	0.617	0.897	646	0.613	0.912	0	0.000	0.000
6	0	0.000	0.000	0	0.000	0.000	0	0.000	0.000
7	566	0.456	0.758	0	0.000	0.000	0	0.000	0.000
8	493	1.236	1.914	518	1.204	1.698	706	1.221	1.842
	319	1.322	1.893	455	1.043	1.429	488	0.923	1.599
9	305	0.951	1.327	0	0.000	0.000	0	0.000	0.000
10	115	0.771	1.086	189	0.816	1.110	272	0.847	1.145
11	0	0.000	0.000	0	0.000	0.000	0	0.000	0.000
12	97	0.956	1.401	223	0.898	1.466	284	0.759	1.171
13	280	0.814	1.111	331	1.044	1.406	0	0.000	0.000
14	145	0.827	1.237	208	0.879	1.480	0	0.000	0.000
15	428	1.577	2.149	0	0.000	0.000	0	0.000	0.000
15	386	1.444	1.893	0	0.000	0.000	0	0.000	0.000
16	130	1.761	2.386	0	0.000	0.000	0	0.000	0.000
17	719	0.920	1.697	0	0.000	0.000	0	0.000	0.000
17	206	1.219	1.757	249	0.954	1.732	0	0.000	0.000
18	372	1.335	1.705	0	0.000	0.000	0	0.000	0.000

Figure A.2: Data table of OCT measurement results for each segment, containing setup and its length, start and end slice, start and end knot and up to four sampled points with slice number as well as the inner and outer radius in mm (segments numbered clockwise beginning at A1 right).

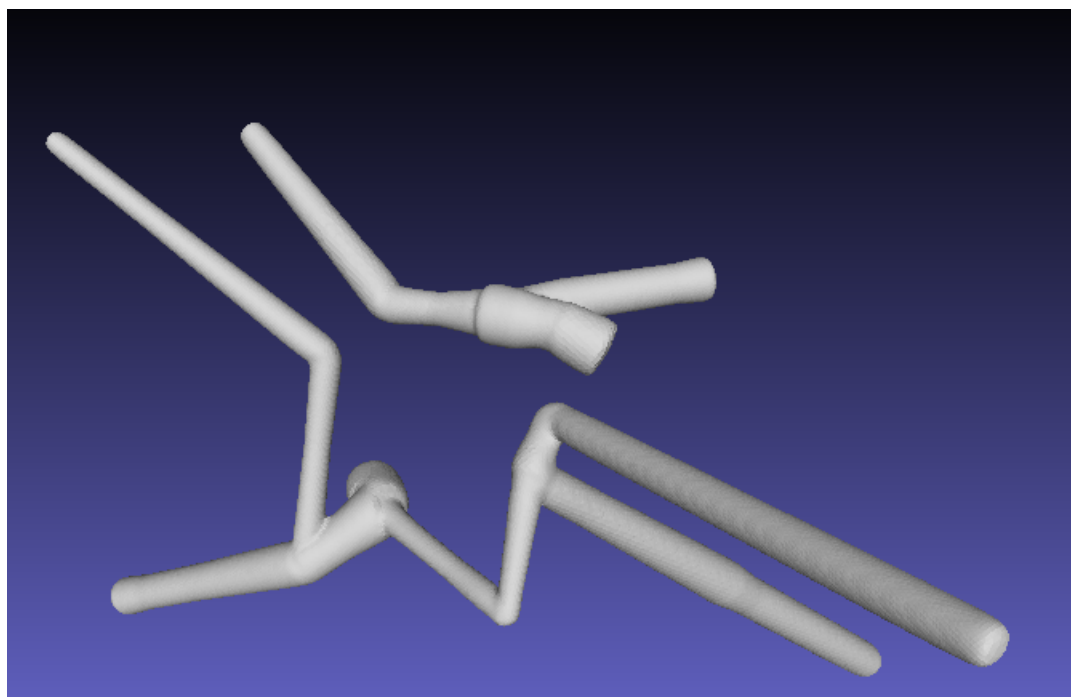


Figure A.3: Post-processed mesh of the outer vessel wall border viewed in MeshLab.



# Bibliography

- [AHDT14] The Alliance Healthcare Deutschland Team. gesundheit.de: Hirnblutungen: Ursachen, Diagnostik, Verlauf. Website, January 2014. Available online at <http://www.gesundheit.de/krankheiten/gehirn-und-nerven/schlaganfall/hirnblutungen-ursachen-diagnostik-verlauf>; visited on Oct 11th, 2015. (cited on Page 3)
- [BBB<sup>+</sup>12] D. Balzani, D. Böse, D. Brands, R. Erbel, A. Klawonn, O. Rheinbach, and J. Schröder. Parallel Simulation of Patient-Specific Atherosclerotic Arteries for the Enhancement of Intravascular Ultrasound Diagnostics. *Engineering Computations*, 29(8):888–906, 2012. (cited on Page 12)
- [Bla] Blausen.com. Blausen gallery 2014. *Wikiversity Journal of Medicine*. Available online at [https://commons.wikimedia.org/wiki/File:Blausen\\_0055\\_ArteryWallStructure.png](https://commons.wikimedia.org/wiki/File:Blausen_0055_ArteryWallStructure.png); visited on January 3rd, 2016. (cited on Page 10)
- [BTP<sup>+</sup>] J. L. Brisman, F. Talavera, R. M. Pluta, B. H. Kopell, and P. L. Penar. Medscape: Neurosurgery for Cerebral Aneurysm. Website. Available online at <http://emedicine.medscape.com/article/252142-overview>; visited on Dec 21st, 2015. (cited on Page 4)
- [Bun10] Statistisches Bundesamt. Gesundheit: Todesursachen in Deutschland. *Fachserie 12*, Reihe 4, 2010. (cited on Page 4)
- [Cip09] M. J. Cipolla. *Anatomy and Ultrastructure*, chapter 2. Morgan & Claypool Life Sciences, 2009. (cited on Page 5)
- [CJL15] Y. J. Choi, S. C. Jung, and D. H. Lee. Vessel Wall Imaging of the Intracranial and Cervical Carotid Arteries. *Journal of Stroke*, 17(3):238–255, 2015. (cited on Page 10)
- [Com] Wikimedia Commons. Circle of Willis. Website. Available online at [https://en.wikipedia.org/wiki/Circle\\_of\\_Willis](https://en.wikipedia.org/wiki/Circle_of_Willis); File: Circle of Willis en.svg, visited on October 11th, 2015. (cited on Page 7 and 20)
- [EW11] Francis Esmonde-White. MATLAB Central File Exchange: Binary STL file reader, 2011. Available online at <http://www.mathworks.com/>

- matlabcentral/fileexchange/29906-binary-stl-file-reader; retrieved on October 9th, 2015. (cited on Page 36)
- [GEE12] C. Gaul, M. Endres, and F. Erbguth. *Harrison's Neurologie*. ABW Wissenschaftsverlag, 2012. (cited on Page 3)
- [GHB<sup>+</sup>15] S. Glaßer, T. Hoffmann, A. Boese, S. Voß, T. Kalinski, M. Skalej, and B. Preim. Histology-Based Evaluation of Optical Coherence Tomographic Characteristics of the Cerebral Artery Wall via Virtual Inflating. *Proc. of Eurographics Workshop on Visual Computing for Biology and Medicine*, pages 149–158, 2015. (cited on Page 11)
- [GLH<sup>+</sup>14] Sylvia Glaßer, Kai Lawonn, Thomas Hoffmann, Martin Skalej, and Bernhard Preim. Combined Visualization of Wall Thickness and Wall Shear Stress for the Evaluation of Aneurysms. *IEEE Transactions on Visualization and Computer Graphics*, 20(12):2506–2515, 2014. (cited on Page 12)
- [GOH<sup>+</sup>10] S. Glaßer, S. Oeltze, A. Hennemuth, C. Kubisch, A. Mahnken, S. Wilhelmsen, , and B. Preim. Automatic Transfer Function Specification for Visual Emphasis of Coronary Artery Plaque. *Computer Graphics Forum*, 29(1):191–201, 2010. (cited on Page 12)
- [HBW<sup>+</sup>10] P. U. Heuschmann, O. Busse, M. Wagner, M. Endres, A. Villringer, J. Röther, P. L. Kolominsky-Rabas, and K. Berger. Schlaganfallhäufigkeit und Versorgung von Schlaganfallpatienten in Deutschland. *Akt Neurol*, 37(7):333–340, 2010. (cited on Page 4)
- [HD09] M. R. Harrigan and J. P. Deveikis. *Handbook of Cerebrovascular Disease and Neurointerventional Technique*. Contemporary Medical Imaging. Humana Press, 2009. (cited on Page 6, 8, and 19)
- [HGB<sup>+</sup>15] T. Hoffmann, S. Glaßer, A. Boese, K. Brandstädter, T. Kalinski, O. Beuing, and M. Skalej. Experimental Investigation of Intravascular OCT for Imaging of Intracranial Aneurysms. *International Journal of Computer Assisted Radiology and Surgery*, pages 1–11, 2015. (cited on Page 11 and 12)
- [HMA13] S. R. Hashemi, R. Mahmoodi, and A. Amirjamshidi. Variations in the Anatomy of the Willis' Circle: A 3-Year Cross-Sectional Study from Iran (2006-2009). Are the Distributions of Variations of Circle of Willis Different in Different Populations? Result of an Anatomical Study and Review of Literature. *Surg Neurol Int*, 4(65), 2013. (cited on Page 8)
- [HSD10] D. M. Hermann, T. Steiner, and H. C. Diener. *Vaskuläre Neurologie: Zerebrale Ischämien, Hämorragien, Gefäßmissbildungen, Vaskulitiden und vaskuläre Demenz*. Thieme-Verlag, 2010. (cited on Page 3)

- [ISCa] The Internet Stroke Center. Blood Vessels of the Brain. Website. Available online at <http://www.strokecenter.org/professionals/brain-anatomy/blood-vessels-of-the-brain/>; visited on Oct 16th, 2015. (cited on Page 7)
- [ISCb] The Internet Stroke Center. Intracerebral Hemorrhage. Website. Available online at <http://www.strokecenter.org/patients/about-stroke/intracerebral-hemorrhage/>; visited on Oct 11th, 2015. (cited on Page 4)
- [KBH06] M. Kazhdan, M. Bolitho, and H. Hoppe. Poisson Surface Reconstruction. In *Proc. of the Eurographics Symposium on Geometry Processing*, pages 61–70, 2006. (cited on Page 30)
- [KWT88] M. Kass, A. Witkin, and D. Terzopoulos. Snakes: Active Contour Models. *International Journal of Computer Vision*, 1(4):321–331, 1988. (cited on Page 43)
- [LGV<sup>+</sup>16] Kai Lawonn, Sylvia Glaßer, Anna Vilanova, Bernhard Preim, and Tobias Isenberg. Occlusion-free Blood Flow Animation with Wall Thickness Visualization. *IEEE Transactions on Visualization and Computer Graphics*, 22(1):728–737, 2016. (cited on Page 12)
- [LO14] P. Lopez-Ojeda. Ultra High Field (7T) Magnetic Resonance Imaging of Intracranial Vessel Wall. *University of Western Ontario: Electronic Thesis and Dissertation Repository*, 2014. (cited on Page 10)
- [Mar09] E. N. Marieb. *Essentials of Human Anatomy and Physiology*. Pearson Education, publishing as Pearson Benjamin Cummings, 2009. (cited on Page 5)
- [MSH<sup>+</sup>11] M. S. Mathews, J. Su, E. Heidari, E. I. Levy, M. E. Linskey, and Z. Chen. Neuroendovascular Optical Coherence Tomography Imaging and Histological Analysis. *Neurosurgery*, 69(2):430–439, 2011. (cited on Page 11)
- [NIH15] NIH National Institute of Health - National Heart, Lung and Blood Institute (US Department of Health & Human Services). Who Is at Risk for Atherosclerosis? Website, 2015. Available online at <http://www.nhlbi.nih.gov/health/health-topics/topics/atherosclerosis/atrisk/>; visited on October 24th, 2015. (cited on Page 9)
- [oNDS13] National Institute of Neurological Disorders and Stroke. U.S. Department of Health and Human Services, 2013. NIH Publication No. 13 5505. (cited on Page 4)
- [RTT<sup>+</sup>11] J. H. C. Reiber, S. Tu, J. C. Tuinenburg, G. Koning, J. P. Janssen, and J. Dijkstra. QCA, IVUS and OCT in Interventional Cardiology in 2011. *Cardiovascular Diagnosis and Therapy*, 1(1):57–70, 2011. (cited on Page 10)

- 
- [TMF<sup>+</sup>12] V. D. Tsakanikas, L. K. Michalis, D. I. Fotiadis, K. K. Naka, and C. V. Bourantas. Intravascular Imaging: Current Applications and Research Developments. *IGI Global*, 2012. (cited on Page 11)
  - [TUBFM] Chair for Virtual Reality Technical University Bergakademie Freiberg, Computer Science Institute and Multimedia. Poisson Surface Reconstruction. Website. Available online at [http://vr.tu-freiberg.de/scivi/?page\\_id=365](http://vr.tu-freiberg.de/scivi/?page_id=365); visited on Nov 18th, 2015. (cited on Page 31)
  - [WHO14] The World Health Organization. The Top 10 Causes of Death. Website, 2014. Available online at <http://www.who.int/mediacentre/factsheets/fs310/en/>; Media Centre: Fact sheet N°310, visited on January 5th, 2016. (cited on Page 1 and 4)
  - [YKY<sup>+</sup>12] S. Yoshimura, M. Kawasaki, K. Yamada, Y. Enomoto, Y. Egashira, A. Hattori, K. Nishigaki, S. Minatoguchi, and T. Iwama. Visualization of Internal Carotid Artery Atherosclerotic Plaques in Symptomatic and Asymptomatic Patients: A Comparison of Optical Coherence Tomography and Intravascular Ultrasound. *American Journal of Neuroradiology*, 33(2):308–313, 2012. (cited on Page 11)

---

Hiermit erkläre ich, dass ich die vorliegende Arbeit selbstständig verfasst und keine anderen als die angegebenen Quellen und Hilfsmittel verwendet habe.

Magdeburg, den 15. Januar 2016